

Crustal Channel Flows: 1. Numerical models  
with applications to the tectonics of the Himalayan-Tibetan Orogen

Christopher Beaumont <sup>1</sup>, Rebecca A. Jamieson <sup>2</sup>, Mai H. Nguyen <sup>1,2</sup>, and Sergei Medvedev <sup>1,3</sup>

<sup>1</sup>Department of Oceanography, Dalhousie University, Halifax, N.S., Canada B3H 4J1

<sup>2</sup>Department of Earth Sciences, Dalhousie University, Halifax, N.S., Canada B3H 3J5

<sup>3</sup>Present address; Freie Universitat Berlin, Fachrichtung Geologie, Malteserstrasse 74-100,  
D-12249 Berlin, Germany

Paper submitted to *Journal of Geophysical Research*, 23 September, 2003

Revised version accepted 10 March, 2004

**Abstract**

Plane-strain, thermal-mechanical numerical models are used to examine the development of mid-crustal channel flows in large hot orogens. In the models, radioactive self-heating reduces the viscosity of tectonically thickened crust and increases its susceptibility to large-scale horizontal flow. Channels can be exhumed and exposed by denudation focused on the high-relief transition between plateau and foreland. We interpret the Himalaya to have evolved in this manner. Channel flows are poorly developed if the channel has a ductile rheology based on wet-quartz flow laws, and well developed if there is an additional reduction in viscosity to  $10^{19}$  Pa.s. This reduction occurs from 700-750°C in the models and is attributed to a small percentage of *in situ* partial melt ('melt weakening'). Model HT1 provides an internally consistent explanation for the tectonic evolution of many features of the Himalayan-Tibetan orogenic system. Erosional exhumation exposes the migmatitic channel, equivalent to the Greater Himalayan Sequence (GHS), between coeval normal- and thrust-sense ductile shear zones, corresponding to the South Tibetan Detachment (STD) and the Main Central Thrust (MCT) systems. Outward flow of unstable upper crust rotates these shears to low dip angles. In the model both the GHS and the Lesser Himalayan Sequence are derived from Indian crust, with the latter from much further south. Similar models exhibit a range of tectonic styles, including the formation of domes resembling north Himalayan gneiss domes. Model results are relatively insensitive to channel heterogeneities and to variations in the behavior of the mantle lithosphere beneath the model plateau.

**Key words:** thermal-mechanical models, Himalayan-Tibetan orogen, crustal channel flow, tectonics, flow modes, surface processes.

## 1. Introduction

An improved understanding of the evolution of large hot orogens, like the modern Himalayan-Tibetan and Andean orogens and their ancient equivalents, is an essential component of research into continental tectonics. Major questions concern the behavior of the lithospheric mantle and styles of crustal deformation and flow. The primary focus of this paper is the style of crustal deformation in large hot orogens with particular emphasis on the development of mid-crustal channel flows.

The potential importance of gravitationally/pressure-driven flows in hot, weak orogenic crust has already been demonstrated [*Bird, 1991; Westaway, 1995; Royden, 1996; Royden et al., 1997; Shen et al., 2001; Clark and Royden, 2000*]. The advance on previous studies offered here and in our earlier work [*Beaumont et al., 2001a,b; Medvedev and Beaumont, 2001*] is to consider these flows in the context of a coupled thermal-mechanical model in which the development of channel flow is linked to and controlled by the thermal evolution of the crust.

The first part of the paper examines how channel flows, driven by the differential horizontal pressure between the internal, thick orogenic crust and external, thin crust, may be initiated as radioactive heating progressively reduces the effective viscosity of the thickened crust and increases its susceptibility to large-scale horizontal flow. This process is illustrated using finite element, vertical cross-section, and thermal-mechanical model experiments. Results from generic reference (type-1) models are used to explore the effects of rheological 'melt weakening' and surface denudation on the development of channel flows. Next, we focus on the interactions among surface denudation, crustal exhumation, and channel flows. This coupling is illustrated in the type-1 models by investigating the model response to surface denudation that is focused on the steep, high-relief transition zone between the interior plateau and exterior foreland. The interactions are

shown to give rise to several possible styles of tectonic behavior, including ductile extrusion and the formation of domes.

The second part of the paper applies these concepts to the Himalayan-Tibetan orogen using models with modified boundary conditions (type 2). Comparisons are made between type-2 model experiments and the inferred evolution of a representative north-south section of the Himalayan-Tibetan orogen. It is shown that models in which a low-viscosity, partially molten, mid-crustal channel is denudationally exhumed to the surface provide an internally consistent explanation for the tectonic exposure of the Greater Himalayan Sequence (GHS) and its relationship to its bounding shear zones, the South Tibetan Detachment (STD) system and the Main Central Thrust (MCT) system. In an accompanying paper, Jamieson et al. [2004] show that the results of a representative channel flow model are consistent with metamorphic and geochronological data from the GHS and the Lesser Himalayan Sequence (LHS), and discuss the present results in the context of other models for the metamorphic evolution of the Himalaya, some of which also include some form of channel flow [e.g., *Grujic et al.*, 1996; *Vannay and Grasemann*, 2001].

## **2. Thermal-Mechanical Model**

The basic design of the finite element thermal-mechanical model is the same as that described in *Jamieson et al.* [2002]. The 2D vertical plane-strain model has two regions; the crust (Fig. 1a,b), in which the velocity and deformation are calculated dynamically, and the mantle, where the velocity is prescribed kinematically (Fig. 1b). The associated model temperature field is calculated for the whole model domain. Thermal-mechanical coupling occurs through the thermal activation of viscous power-law creep (Fig. 1). Model parameters and values are given in Table 1. We first describe the mantle kinematics for the type-1 models (section 3) and later introduce variations considered more appropriate for the Himalayan-Tibetan orogen (type-2 models; section 4). In type-

1 models (Fig. 1), the pro-mantle lithosphere converges at a uniform velocity,  $V_P$ , and detaches and subducts beneath the stationary,  $V_R = 0$ , retro-mantle at  $S$  [Willett *et al.*, 1993] (Fig. 1b). The corresponding velocity boundary condition applied to the base of the model crust in the mechanical model therefore changes from  $V_P$  to zero across the detachment point  $S$  (Fig. 1a). The subducted mantle lithosphere descends into the mantle with constant velocity as a slab with constant dip,  $\theta$ , (Fig. 1b).

The 2D plane-strain mechanical model used to calculate the velocity field and deformation [Fallsack, 1995] uses an Arbitrary Lagrangian Eulerian (ALE) methodology in which creeping flows with free upper surfaces and large deformation are calculated on an Eulerian finite element grid that evolves to conform to the material domain. A Lagrangian grid, which is advected with the model velocity field, is used to update the mechanical and thermal material property distributions on the Eulerian grid as their position changes. Flow is driven by the basal velocity boundary conditions described above (Fig. 1a).

The corresponding thermal evolution includes diffusion, advection and radioactive production of heat and is calculated on the same Eulerian finite element mesh by solving the heat balance equation.

$$\rho C_p \partial T / \partial t + \underline{v} \cdot \nabla T = K \nabla^2 T + A$$

where  $\rho$  is density,  $C_p$  is specific heat,  $T$  is temperature,  $t$  is time,  $\underline{v}$  is velocity,  $K$  is thermal conductivity and  $A$  is radioactive heat production per unit volume. The advection velocities are those prescribed kinematically in the mantle and calculated dynamically in the crust. The flexural isostatic compensation resulting from changes in crustal thickness is calculated from the elastic flexure of a beam embedded in the model at the base of the crust.

The surface denudation model is designed as a simple approximation of a fluvially controlled regime. The denudation rate is proportional to product of the local slope, and a spatial climate function,  $g(x)$ , and is modulated with a time function,  $f(t)$  (Fig. 1). To a first approximation  $g(x)$  is a measure of the spatial variation of aridity (0 = dry, 1 = wet) across the model, and  $f(t)$  combines the effects of long term climate variations, the bedrock incision rate constant, and a parameter that scales the model surface slopes, which are determined on a 10 km spatial resolution, to include higher riverbed slopes at smaller scales. A more detailed denudation model is not justified because the model is cross-sectional, and therefore cannot represent planform drainage patterns, and the scaling effect in  $f(t)$  for local slopes at less than 10 km spatial resolution is not known accurately. Explicitly, the rate of denudation at a given surface node on the Eulerian finite element grid is

$$\dot{\epsilon}(t,x) = \text{slope} \times f(t) \times g(x)$$

where slope is the average of the surface slopes of the two elements adjacent to the node. These slopes change as the model evolves. The climate function  $f(t)$  (Table 1) is scaled to give reasonable denudation rates of the order 0.1 to 2.0 cm/yr for the parts of the model orogen that are considered to be subject to strong orographically charged fluvial denudation. This scaling changes with time to produce phases of relatively higher and lower denudation rate. When better data are available the value of  $f(t)$  can be calibrated for a particular orogen or part of an orogen. The spatial function,  $g(x)$  has a value 1.0 where orographically charged denudation is considered to be most efficient, that is, on the windward flank of the model orogen. The value of  $g(x)$  is reduced to values as low as 0.0 on the model plateau and on the downwind flank of the model orogen (Table 1). The model result figures have insets showing  $\dot{\epsilon}(t,x)$ , that is the current distribution of the rate of denudation in cm/y across the model. The values of  $f(t)$  and  $g(x)$  for each of the models are given in Table 1.

The finite-element model uses a viscous-plastic rheology. The plastic (frictional or brittle) deformation is modeled with a pressure-dependent Drucker-Prager yield criterion. Yielding occurs when

$$(J_2')^{1/2} = c + p \cdot \text{Sin} \phi_{eff}$$

(see Table 1 for symbols) where the value of  $\phi_{eff}$  is defined to include the effects of pore fluid pressures through the relation

$$p \cdot \text{Sin} \phi_{eff} = (p - p_f) \cdot \text{Sin} \phi$$

where  $\phi = 30^\circ$  for dry frictional sliding conditions (approximately Byerlee's law conditions) when the pore fluid pressure,  $p_f = 0$ .

The incompressible plastic flow becomes equivalent to a viscous flow if an effective viscosity,  $\eta_{eff}^p$  is defined for the plastic material [Fullsack, 1995; Willett, 1999] such that

$$\eta_{eff}^p = (J_2')^{1/2} / 2(\dot{I}_2')^{1/2}.$$

Setting the viscosity to  $\eta_{eff}^p$  in regions that are on frictional-plastic yield satisfies the yield condition and allows the velocity field to be determined from the finite element solution for viscous creeping flows. The overall non-linear solution is determined iteratively using  $\eta = \eta_{eff}^p$  (for regions of plastic flow) and  $\eta = \eta_{eff}^v$ , as defined below (for regions of viscous flow).

When the stress is below frictional-plastic yield flow is viscous. The power law creep effective viscosity,  $\eta_{eff}^v$  is given by

$$\eta_{eff}^v = B^* \cdot (\dot{I}_2')^{(1-n)/2n} \cdot \exp[Q/nRT_K]$$

and the values of  $B^*$ ,  $n$ , and  $Q$  are based on laboratory experiments (Table 1) with 'A' values converted to  $B^*$  assuming cylindrical creep tests. The rheology of the upper crust (0-25 km in the

initial configuration) is based on the 'wet Black Hills quartzite' flow law [Gleason and Tullis, 1995]. In the model experiments (Table 1) the value of  $B^*$  is scaled by constants with values ranging from 5 to 0.1 to represent crust that is somewhat higher or lower viscosity than the standard Gleason and Tullis [1995] flow law. This scaling is permissible given the range of power-law creep properties for quartz-rich upper crustal rocks and allows us to investigate the model sensitivity to a range of upper crustal properties. The rheology of the lower crust (25-35 km initially) is based on the 'dry Maryland diabase' flow law [Mackwell *et al.*, 1998] (DMD, Table 1). In some experiments this value of  $B^*$  is also scaled. The rheological structure can be considered to represent a two-layer crust comprising quartzo-feldspathic rocks underlain by an intermediate dry granulitic lower crust. Later we introduce a third layer of weaker surface sediments (section 3) and also consider the effect of weaker lower crust (section 7).

The most important additional model property is an extra increment of viscous weakening in the upper crustal material such that the effective viscosity decreases linearly with temperature from the dynamically determined power law creep value at 700°C to  $10^{19}$  Pa.s at 750°C and higher temperatures. This weakening is an approximation to the reduction in the bulk viscosity which will be caused by a small amount of *in situ* partial melt. The 'weakening' amounts to approximately a factor of 10 decrease in effective viscosity. This is probably a conservative estimate for what we term 'melt weakening'. In the models lower crust does not 'melt weaken' because it is considered to have undergone earlier granulite facies metamorphism and will therefore be depleted and not prone to melting. It is also true that the temperatures achieved in the models would be insufficient to cause melting if an intermediate or mafic composition is assumed. In all instances the model deforms according to the mechanism that produces the lowest level of the second invariant of the deviatoric stress for the prevailing conditions.

Both the mechanical and thermal calculations are carried out for each timestep (Fig. 1). The upper 20 km of the crust has a uniform radioactive heat production,  $A_1 = 2.0 \mu\text{Wm}^{-3}$  which is higher than the corresponding heat production,  $A_2 = 0.75 \mu\text{Wm}^{-3}$  in the lower crust [Jamieson *et al.*, 2002]. For each model run, the initial steady-state temperature field is calculated at the lithospheric scale with a basal heat flux,  $q_m = 20 \text{ mW/m}^2$ , a surface temperature of  $0^\circ\text{C}$ , and no heat flux through horizontal side boundaries. The lithosphere-asthenosphere boundary is defined to be at the  $1350^\circ\text{C}$  isotherm. For these conditions and thermal conductivity,  $K = 2.00 \text{ W/m}^\circ\text{K}$  the initial surface heat flux  $q_s = 71.25 \text{ mW/m}^2$ , and the Moho temperature is  $704^\circ\text{C}$  (Fig. 1).

The effect of a precursor phase of oceanic subduction, which is included in some of our models [e.g. Vanderhaeghe *et al.*, 1999], is not included here because it has little effect on the evolving crustal temperatures and peak metamorphic conditions in these models which consider long periods of orogenesis after oceanic subduction terminates [Jamieson *et al.*, 2002]. All models are, however, run for an initial set-up phase without surface denudation. This is designed to achieve a model state with an embryonic plateau and mid-crustal channel flow as a precursor to denudation. The results are similar when moderate denudation occurs during the set up phase but the times to develop the plateau and channel flow are somewhat longer.

### **3. Type-1 Models: Experiments with $V_P = 2 \text{ cm/y}$**

#### **3.1 Reference Model 1: 2-layer, melt-weakened crust with minimum viscosity $10^{19} \text{ Pa.s}$**

We first describe results from a reference model, Model 1 (Figs. 2, 3; Table 1) and then develop subsequent models by systematically varying a few important parameters (Table 1). Model layers and corresponding rheological and thermal parameters are described above and shown in Figure 1 and Table 1. Type-1 models have  $V_P = 2 \text{ cm/y}$ ,  $V_R = 0$ , and the S-point remains stationary,

$V_S = 0$ . The initial set-up phase (no denudation) ends at 37.5 My.

The evolution of Model 1 during the initial 30 My (Fig. 2) shows the deformation of a Lagrangian marker grid and the crustal layers, distribution of radioactive heat sources, and velocity and temperature fields. The corresponding evolution of the model topography is shown for the entire model in Figure 4. Vertical lines in the marker grid are numbered with '0', representing the model 'suture', initially located above the S-point. In regions where the crust has not thickened the velocity is uniform with depth but viscous decoupling occurs between the upper and lower crust as the crust thickens. The lower crust remains coupled to the kinematically prescribed mantle lithosphere except in the vicinity of S. Variations in the crustal velocities across the S-point reflect the degree of coupling between the upper crust, lower crust, and upper mantle lithosphere (Fig. 2a,b). By 22.5 My (Fig. 2c) a mid-crustal velocity minimum develops pro-ward of the S-point and by 30 My (Fig. 2d) there is evidence of incipient counterflow in melt-weakened upper crust.

The deformation shown by the marker grid (Fig. 2) illustrates growth of an asymmetric antiform of thickened lower crust above S (Fig. 2b) that is progressively transported retro-ward together with the upper crust by an amount measured by the offset of the 'suture' (marker '0') from S (e.g. Fig. 2d). This lower crustal wedge forms when the lower pro-crust is not subducted with the underlying pro-mantle lithosphere. The presence of similar regions of thickened lower crust in natural orogens should therefore be a good indicator that the primary detachment level in continental lithosphere is at least as deep as the Moho. Conversely, their absence suggests that lower crust may be subducted. Later we use this result to justify subduction of the lower pro-crust in type-2 models.

The thermal structure of the model (Fig. 2) is closely linked to the evolving distribution of thickened radioactive crust. Temperatures initially rise in the thickening crust and are lowered in

the vicinity of the subducting mantle lithosphere. However, by 22.5 My radioactive heating dominates and much of the middle and lower crust in the orogenic core is above 700°C (Fig. 2c). At this time the velocity minimum in the pro-crust occurs where temperatures are below 700°C and, therefore, corresponds to low viscosity flow according to the wet-quartzite flow law rather than to the melt-weakening effect.

The set-up phase of Model 1 ends with the onset of denudation at 37.5 My. The subsequent evolution of the model demonstrates the interaction between the channel flow and denudation focused at the sloping pro-flank of the plateau. The climate function precludes denudation on the corresponding retro-flank (Fig. 1, Table 1).

Between 45 and 60 My (Fig. 3) channel flow initiates in the thickened upper crust where temperatures are between 700° and 750°C, corresponding to the region where melt-weakening reduces the viscosity to a minimum of  $10^{19}$  Pa.s. The lower crust, which is not influenced by melt-weakening, does not participate in the channel flow. By 45 My, a 15 km thick channel is well developed but the flow tip is still a long way from the denudation front (Fig. 3a). A plateau develops above the channel and the retro-wedge (Fig. 4) because both of these regions are now sufficiently hot ( $>800^{\circ}\text{C}$ , Fig. 3a) and weak that the crust cannot maintain lateral topographic gradients. By 52.5 My, the channel has expanded outward beneath the plateau and its tip is nearing the denudation front. We refer to the expansion as 'tunneling' by the channel because it involves the incorporation of crustal material into the channel. This process is discussed in more detail in section 9. It can, however, be seen from Figure 3b that the crustal temperature has to be between 700 and 750°C for the channel flow to develop either in an instantaneous sense, or to create finite tunneling. That is, thermal weakening of the thickened crust is required as a precursor to channel tunneling. The upper pro-crust above the channel is also translated toward the denudation front (Fig. 3b, note

the contrast with Fig. 3a). Crust therefore converges laterally on the denudation front from both directions (Fig. 3b). The strong lower crust is, however, unaffected by the denudation and continues to underthrust the channel without deformation at locations pro-ward of S. At this stage the maximum denudation rate is approximately 6 mm/y (Fig. 3b). Isotherms are bowed upward at the denudation front and condensed into a thin high-gradient boundary layer owing to thermal advection by material moving upward beneath the denudation front to replace eroded material (Fig. 3b). In the mid-crust isotherms are advected laterally and inverted by the channel flow, resulting in a near-isobaric temperature increase from 600° to 900°C between the edge of the plateau and the S-point at the level of the channel (Fig. 3b).

By 60 My there is strong coupling between the channel flow and the denudation front (Fig. 3c). The focused denudation exhumes channel material to the surface in a narrow, nearly symmetric zone. Converging pro-crust is deformed, rotated and exposed at the surface in the footwall beneath the channel material. Correspondingly, a cross-section of plateau-edge upper crust is exposed in the hangingwall above the channel (Fig. 3c). The extruded channel is bounded by upper normal-sense and lower thrust-sense shear zones. Isotherms are advected upward and outward by the flow as the channel is exhumed, forming a thermal boundary layer in which 700°C crust lies at a depth of only 15 km when denudation rates peak at approximately 1 cm/y.

At 60 My, the retro-side of the model (Fig. 3d) is still in the process of transition to a plateau [e.g., *Vanderhaeghe et al.*, 2003]. The suture has been transported progressively retro-ward and its surface expression is now located more than 300 km from S. Consequently, approximately half the retro-crust comprises material advected from the pro-side of the orogen (*i.e.* material above the trace of the suture, Fig. 3d ). There is no channel flow in the thickened lower crust but a weak channel has developed in the hot mid-crust. In the absence of denudation, the channel tunnels

outward at a rate determined by the timescale that radioactive self-heating and thermal relaxation of the thickening crust take to weaken the crust. By 75 My (partly shown in Fig. 5) a retro-plateau has developed and the plateau edge, plateau flank, and channel tip achieve a steady-state geometry with respect to each other as the orogen grows outward. Tectonic shortening of the upper crust and inflation by channel material both contribute to the crustal thickening across the foreland to plateau transition.

The total velocity field of the model can be decomposed into components driven by the velocity boundary conditions and by gravity (Fig. 5). This is done by taking the converged nonlinear solution and then re-solving for the boundary and gravitational forcing separately without changing the converged model properties. The flow caused by the boundary conditions is consistently retro-ward, although it is greatly reduced in the hottest part of the channel flow zone. In contrast, gravitational flow is in the pro-direction, i.e. a counterflow, on the pro-side of the system, and is a maximum in the channel. The velocity decomposition therefore demonstrates that gravity drives the channel flow through the pressure gradient caused by the lateral variation in the weight of the channel overburden [cf. *Turcotte and Schubert*, 1982, p.234].

### **3.2 Effects of Variations in Parameter Values**

Models 2, 3, 4, and 5 (Figs. 6, 7) illustrate the effects of no erosion, no melt weakening, a lower value of the minimum melt-weakened viscosity, and the role of a weaker upper crustal rheology on the tectonic style of the reference model (Model 1). All other model parameters remain the same.

Model 2 illustrates tunneling by the channel flow in the absence of erosion. Channel counterflow initiates at 30 My (Fig. 2) and the channel tip tunnels outward through the pro-crust as a plateau develops above. The rate of tunneling and the channel velocity are both less than in

Model 1 and the propagation of the channel is again limited by the need to heat and weaken the tectonically thickened crust. Crustal thickness reaches a maximum of approximately 75 km by 45 My; by 75 My the large-scale geometry is similar to Model 1 although there is no surface evidence of the underlying channel flow. Lateral expansion of the channel into the converging pro-crust leads to surface shortening across the plateau flank, but little added deformation within the plateau. Models with denudation rates intermediate between those in Models 1 and 2 (not shown) partly exhume and expose the channel material.

In Model 3 there is no melt-weakening and, therefore, the viscosity of the upper and mid-crust is controlled by the wet-quartzite flow law (Table 1, Fig. 1 WQ x 5). The channel does not develop until ca. 52 My because temperatures must exceed 850°C before the viscosity is sufficiently reduced. By comparison with Model 1, channel counterflow is sluggish and the channel tip tunnels slowly. At approximately 67 My, the velocity field changes and the entire plateau pro-crust above the channel translates outward with the channel. The two types of channel flow, flow between stationary boundaries and flow with moving boundaries, are respectively known as Poiseuille and Couette flows [e.g. *Turcotte and Schubert*, 1982, p.234], as discussed further below (section 9). We refer to the outward translation of the upper crust as an unstable flow because it is caused by a gravitational instability of the crust above the viscous channel. The velocity of the translation is partly controlled by the viscous coupling between these two regions. This mechanism would lead to what has been termed 'gravitational collapse'. The outward flow of unstable upper crust extends and thins the plateau crust in the region above the lower crustal antiform and slightly increases the rate of shortening at the denudation front. There is less coupling between surface denudation and the channel flow (cf. Model 1 at 52.5 My; Fig. 3); at 75 My the channel tip still underlies the plateau

although a broad, symmetrical exhumation zone (cf. Model 1, 60 My; Fig. 3) is evident on the plateau flank

In Model 4 the effect of melt-weakening is enhanced by decreasing the minimum effective viscosity from  $10^{19}$  Pa.s at  $750^{\circ}\text{C}$  to  $2 \times 10^{18}$  Pa.s. Crustal velocities, deformation, and thermal fields evolve in a similar manner to those of Model 1 (Figs. 3, 5, 6), and the velocity field, decomposed into boundary and gravitationally forced components, is also similar to that in Model 1 (Figs. 5, 6). In infinitely long channel flows [e.g. *Turcotte and Schubert, 1982*], the gravitationally induced velocity is predicted to scale with the inverse of the viscosity. A comparison of Models 1 and 3 shows a much smaller difference than predicted, because the high viscosity crust at the end of the channel impedes the flow, an effect not considered in simple unrestricted channel models. This result highlights the potential importance of thermal-mechanical coupling in limiting crustal channel flows, a point addressed in section 9.

Model 5 tests model sensitivity to the presence of a weak upper crust, approximating an unmetamorphosed sedimentary sequence above crystalline middle crust. The weak upper crustal layer affects the model because it may become unstable under the basal drag from the channel counterflow, particularly when it is progressively thinned by erosion at the denudation front. In Model 5 the internal angle of friction ( $\phi_{eff}$ ) of the upper 10 km of crust is reduced to  $5^{\circ}$ , which can be interpreted to represent moderate overpressuring by pore fluids. Otherwise the model is the same as Model 1, and initially evolves in a similar way. However, focused erosion at the denudation front, which thins and weakens the upper crust further, leads to a transition from stable to unstable upper crust between 60 and 67.5 My (Fig. 7). In this case the gravitational instability of the channel and overlying crust is sufficient that the outward translating upper crust overrides the exhumation front (Fig. 7; cf. Model 3, Fig. 6b), creating an asymmetric, thrust-sense extrusion zone. This type

of behavior is discussed in more detail below (type-2 Model HT1). The outward translation of the upper crust also causes the plateau crust adjacent to the lower crustal antiform to extend and thin, allowing upwelling of the low viscosity channel material (Fig. 7) in a broad dome-like region beneath the plateau.

#### **4. Type 2 Models: Himalayan-Tibetan Style Experiments**

In the second part of the paper we compare model results with a representative north-south cross section of the Himalayan-Tibetan orogen (Fig. 8; sources cited in caption). The purpose of the comparison is to show that a representative type-2 model (HT1), in which a low viscosity, mid-crustal channel is exhumed to the surface by erosion, provides an internally consistent explanation for the large-scale geometry and tectonic features of the Himalaya and southern Tibet (Fig. 8b). In particular, we consider the rapid erosion of the southern flank of the Himalaya, the surface position of the Indus-Tsangpo suture, the origin of the GHS, including the mechanism for its uplift and exposure and its relationship to its bounding shear zones (STD and MCT), the tectonic processes that juxtaposed the GHS and LHS across the MCT zone, and the origin of the north-south extension in the southern Tibetan plateau and associated north Himalayan gneiss domes. We also demonstrate model response, and corresponding tectonic styles, to variations in denudation rates, crustal strength, and assumed mantle kinematics. Some of these tectonic styles may currently exist in parts of the Himalayan-Tibetan system, or may have existed at earlier stages of its development. In the accompanying paper *Jamieson et al.* [2004] test predictions from model HT1 against a variety of metamorphic and geochronologic data from the GHS and LHS in the central part of the orogen.

##### **4.1 Type-2 Models: Primary Assumptions**

The simplifying assumptions used in the HT model experiments are as follows. The boundary conditions do not change with time, and there is no movement of crust normal to the cross section.

In the Himalayan-Tibetan system the cumulative out-of-plane flow of material has been estimated to be approximately 15-30% of the total convergence [Dewey *et al.*, 1988; Le Pichon *et al.*, 1992; Westaway, 1995; but also see Johnson, 2002] and GPS data suggest that this flow is currently significant [Wang *et al.*, 2001]. Its importance for modeling the Himalayan-Tibetan orogen can be assessed from Royden *et al.* [1997] and Shen *et al.* [2001].

Resorption of lithosphere by the mantle under large hot orogens, and beneath the Himalayan-Tibetan orogen in particular, is poorly understood and may involve subduction and/or underthrusting [e.g., Owens and Zandt, 1997], downwelling [Tilmann *et al.*, 2003], delamination [Bird, 1978] and/or slab break-off and/or slab retreat [e.g., Willett and Beaumont, 1994; Van der Voo *et al.*, 1999; Mahéo *et al.*, 2002], or convective removal [e.g., Houseman *et al.*, 1981; Molnar *et al.*, 1993]. Here, we initially assume that subduction and/or underthrusting dominates and also consider migration of the S-point as described below. Royden *et al.* [1997] and Shen *et al.* [2001] showed that these boundary conditions are compatible with the planform evolution of the orogen. Results presented here complement theirs by providing a more complete analysis of the plane-strain thermo-mechanical evolution. Although the subduction boundary condition may not be correct, in section 8 we demonstrate that for the region of interest (pro-ward of the model suture) the model results are relatively insensitive to this particular choice. We also assume that the lower pro-crust remains attached to, and is subducted with, its underlying mantle lithosphere. Subduction of lower pro-crust is preferred because in Tibet there is no known large lower crustal antiform, as seen in the previous models (e.g., Fig. 3) and, therefore an alternative sink for lower crust is required.

For simplicity, we first investigate models with laterally uniform initial mechanical and thermal properties. In section 7 we consider the effects of crustal heterogeneity.

## 4.2 Type-2 Models: Advancing Subduction Boundary Condition

In Type 2 models the boundary conditions are chosen to be compatible with the average 5 cm/y post-collisional convergence rate ( $\underline{V}_P$ ) in the Himalayan-Tibetan orogen (Fig. 9; *Dewey et al.*, 1988; *Searle*, 1996; *Hodges*, 2000; *Hauck et al.*, 1998). In both nature and the models, the S-point location (Fig. 1) may migrate, leading to subduction zone advance (Fig. 9) or retreat [*Royden*, 1993; *Willett and Beaumont*, 1994; *Waschbusch and Beaumont*, 1996]. Evidence for advancing subduction in the Himalayan-Tibetan orogen comes from the manner in which pre-collisional suture zones north of the Tsangpo suture wrap around India [*Dewey et al.*, 1988]. This geometry is compatible with crustal deformation driven by northward-advancing subduction [*Royden et al.*, 1997] and relict slabs imaged by tomography [*Van der Voo et al.*, 1999; *DeCelles et al.*, 2002]. We show below that models with advancing subduction are compatible with the current surface position of the Tsangpo suture, whereas stationary S-point models (Fig. 9a) are not. In the pro-/retro-/S-point terminology, advance of the S-point ( $\underline{V}_S$  same direction as  $\underline{V}_P$ ; Fig. 9b) implies that convergence of the pro-lithosphere is partitioned between subduction zone advance, at rate  $\underline{V}_S$ , and subduction, at rate  $\underline{V}_P - \underline{V}_S$ . Figure 9 also shows the advancing subduction boundary condition applied at the base of the crust (Fig. 9b), and combined with subduction of the lower pro-crust (Fig. 9c). In the Himalayan-Tibetan models described below,  $\underline{V}_P = 5$  cm/y,  $\underline{V}_S = 2.5$  cm/y, and  $\underline{V}_R = 0$ , chosen from a sensitivity analysis and also compatible with the position of the inferred Tethyan relict slab [*DeCelles et al.*, 2002].

From the perspective of the tractions exerted at the base of the crust, any transformation that preserves the two independent velocities,  $\underline{V}_P - \underline{V}_S$  and  $\underline{V}_R - \underline{V}_S$  (Fig. 9), produces equivalent boundary conditions. For example, a fixed S-point reference frame model equivalent to that shown in Figure 9b is obtained by subtracting 2.5 cm/y from all velocities. In this reference frame,

subduction at the S-point can be interpreted to be symmetric, involving both mantle lithospheres. Similarly, subtracting 5 cm/y from all velocities changes the reference frame to one in which India is fixed and the S-point retreats as Indian mantle lithosphere subducts. The mechanics of crustal deformation in all of these models is the same, which implies that in equivalent natural orogens information on the crustal deformation alone is insufficient to allow  $\underline{V}_P$ ,  $\underline{V}_S$ , and  $\underline{V}_R$  to be determined independently. Additional constraints, such as slab dip, the thermal effect of the mantle on the crust, or independent estimates of velocities with respect to an external reference frame, are required to remove this uncertainty. For the Himalayan-Tibetan system, we prefer to interpret the results in the fixed Asia reference frame (Fig. 9b,c). However, to minimize the width of subsequent figures, the results (e.g. Fig. 10) are shown with a fixed S-point.

## 5. Model HT1

Model HT1 is a representative channel-flow model that produces results in broad agreement with generalized observations from the Himalayan-Tibetan orogen. Except for the advancing S-point and subduction of lower pro-crust, the initial configuration of HT1 is the same as Model 5 above (Fig. 1), with three laterally uniform crustal layers [Fig. 1 of *Jamieson et al.*, 2004]; its properties are also similar to Model 3 of *Beaumont et al.* [2001b] except that Model 3 had a weaker upper crust  $B^*(WQ/2)$  versus  $B^*(WQ)$  in HT1. Model HT1 represents the end member in which denudation is focused on the pro-flank of the model orogen, the region corresponding to the Himalayan front, with no denudation of the interior plateau or of the northern retro-flank of the system. However, similar results are obtained for the pro-side of the model when there are low denudation rates on the retro-flank. Advancing subduction requires removal of the retro-mantle lithosphere, which we model by subduction/ablation of the retro-mantle lithosphere [*Tao and O'Connell*, 1992; *Pope and Willett*, 1998; see mantle kinematics, Fig. 1 of *Jamieson et al.*, 2004],

in order to conserve mantle lithosphere. To allow for uncertainties in age, total convergence, and convergence velocity, current Himalayan-Tibetan properties should be compared with the model results in the range 48-54 My. Here we focus on the tectonic results; the corresponding thermal and metamorphic results are described in *Jamieson et al.* [2004].

Model HT1 evolves like Model 5, with corresponding phases of channel counterflow beneath stable upper crust, coupling between the channel and the erosion front, instability of the upper pro-crust above the channel, and finally outward flow of the upper crust together with the underlying channel, leading to overthrusting and asymmetry at the erosion front. Both models have similar thermal and tectonic styles in the region corresponding to the Himalaya and southern Tibetan plateau, although they develop at different times because the convergence velocities differ. The similarities demonstrate that this region of the model is insensitive to the difference between the boundary conditions for the two types of model experiments. The predicted tectonic styles are also similar to that of the Himalayan front (Fig. 8). Models 5 and HT1 do, however, differ in regard to the respective presence and absence of the large lower crustal antiform at the S-point (Figs. 7, 10), because the lower crust is not subducted in Model 5.

### **5.1 Effect of Boundary Conditions on Suture Migration**

Models 5 and HT1 also differ in regard to the evolution of the surface position of the suture (marker '0', Figs. 7, 10). When  $\underline{V}_S = \underline{V}_R = 0$  (type-1 models), the orogenic crust is mostly derived from the pro-lithosphere and, consequently, the surface position of the suture is transported progressively retro-ward with respect to the S-point (Figs. 2, 7). This process would create a mid/upper Tibetan crust composed primarily of Indian plate crust, contrary to observation [e.g. *Yin and Harrison, 2000; DeCelles et al., 2002*]. In contrast, when type-2 boundary conditions are used as in Figure 9b, the orogenic crust is derived approximately equally from both sides of the system.

This result is easily understood in the fixed S-point reference frame ( $\underline{V}_S = 0$ ) in which crustal convergence is symmetric above the S-point. Therefore, in the absence of denudation, the surface position ('0') of the suture (Su) in a model like that shown in Figure 9b, remains above the mantle suture (S-point) and would be located in the center of the orogen, corresponding to the middle of the Tibetan plateau in the Himalayan-Tibetan context. This result remains approximately the same in a model in which lower pro-crust subducts, corresponding to HT1 but with no denudation. In summary, the tectonically driven motion of the surface suture with respect to the S-point is retro-ward if  $|\underline{V}_P - \underline{V}_S| > |\underline{V}_R - \underline{V}_S|$  and the converse if the inequality is reversed.

## 5.2 Effect of Denudation on Suture Migration

Denudation also causes the surface position of the suture to migrate. This is because it removes material and adds a second source of imbalance in the crustal material fluxes, in addition to the one from the basal boundary conditions. In model HT1 the surface and mantle sutures remain aligned, as explained above (Fig. 10a), until asymmetric denudation of the pro-flank of the orogen causes progressive pro-ward translation of the surface suture (Fig. 10b-d). The resulting position of the surface suture at 51-54 My (Fig. 10d, '0') corresponds well to the equivalent average position the Indus-Tsangpo suture in the Tibetan plateau (Fig. 8). The combination of the choice of  $\underline{V}_S$  and cumulative denudation in HT1 therefore reproduces the observed surface suture position. However, this choice is not unique because there is a tradeoff between the two processes. HT1 probably represents the end member in which  $\underline{V}_S$  is a minimum and cumulative denudation is a maximum. Equivalent results could be achieved with  $\underline{V}_S > 2.5$  cm/y and less cumulative denudation. For example, *Willett and Beaumont* [1994] favored the higher  $\underline{V}_S$  boundary condition and interpreted the behavior in terms of subduction zone retreat of the Asian mantle lithosphere. That is, when  $\underline{V}_S > 2.5$  cm/y Asian mantle lithosphere is subducted/ablated more rapidly than Indian mantle

lithosphere. Models with  $\underline{V}_S > 2.5$  cm/y may be shown to be preferable once an accurate estimate of the total denudational mass per unit cross-sectional length of the orogen can be made. The converse,  $\underline{V}_S < 2.5$  cm/y with more cumulative denudation, is probably not acceptable because this would require unreasonably high average denudation rates throughout the development of the orogen. The tradeoff between  $\underline{V}_S$  and denudation has implications for the thermochronology of exhumed rocks [Jamieson *et al.*, 2004].

### 5.3 Crustal Geometry and Properties

Model HT1 has properties consistent with the observed Himalayan-Tibetan orogen in regard to crustal thickness, plateau width, and extent of underthrusting of pro-mantle lithosphere (Figs. 8, 10; similar to Model 3 of *Beaumont et al.*, 2001b). The long-wavelength topography (Fig. 11) develops first by uplift of the surface adjacent to the suture to levels equal to or greater than the eventual plateau height (e.g., Model 1, Fig. 2). This region of high elevation then propagates outward in both directions and forms a plateau as the mid-crust becomes hot and weak [Royden, 1996; *Beaumont et al.*, 2001b; *Vanderhaeghe et al.*, 2003]. By implication, in planform the plateau expands outward from a high, linear, narrow core, as predicted by *Shen et al.* [2001], and is not created by late-stage 'plateau uplift' over a broad region. The testable prediction is that locations close to the Indus-Tsangpo suture have had persistently high elevations, perhaps even higher than today, throughout Cenozoic Himalayan-Tibetan orogenesis [e.g., *Rowley*, 2002; *Spicer et al.*, 2003].

At this point the provenance of channel material is worth noting. Channel material is derived from two sources. Initially, melt-weakening occurs in mid-crustal material located just pro-ward of the S-point. This is shown by comparing the channel position with the location of the model suture and its trace with depth (vertical marker '0', Fig. 10a), which represents the boundary between pro-

and retro-crust. Material located pro-ward of this line is equivalent to Indian crust. Later, as the suture is advected pro-ward (Fig. 10b-d), material from retro-ward of the suture, equivalent to Asian crust, is advected in the channel across the S-point. However, even at 54 My this material remains close to or retro-ward of the surface location of the suture (Fig. 10d). The results therefore predict that exposed channel mid-crust located pro-ward of the Indus-Tsangpo suture (Fig. 8 and marker '0', Fig. 10) will have Indian crustal characteristics; in contrast, retro-ward of the surface suture, exposed mid-crustal rocks and plutons derived from melting of the crust should exhibit Asian affinities. The GHS, having been derived from the mid-crust of the leading edge of the pro-lithosphere, is predicted to have Indian crustal characteristics, a result that is consistent with geological observations [e.g. *DeCelles et al.*, 2002; *Myrow et al.*, 2003].

## **6. Effects of Denudation Rate and Upper Crustal Strength: Tunneling, Extrusion, and Doming**

The models illustrated in Figures 12 and 13 all have the same advancing subduction boundary conditions as HT1, but variations in surface denudation rate and upper crustal strength lead to a variety of predicted deformation styles. Both upper crustal rheology and denudation contribute to the stability of the crust above the channel and to the geometry of the exhumation/thrust front. In the limit of no denudation and moderately strong upper crust, the channel tunnels outward into the converging crust (Fig.12a). However, significant erosion of the model plateau flank produces five different tectonic exhumation and doming styles, resulting from interactions among denudation, upper crustal deformation, and the channel flow.

### **6.1 Near-Symmetric Exhumation**

Denudation of the plateau flank leads to exhumation of the channel as material is removed from the surface. Active channel flow will continue during exhumation if the channel viscosity

remains low, which depends on the cooling rate during exhumation. Rapid denudation and exhumation remove surface material at high thermal Peclet number and the channel is advected upward with little cooling. The same advection also thins the surface thermal boundary layer and weakens the upper crust. The positive feedback between denudation and channel exhumation is reinforced by other processes that weaken the crust. For example, high pore fluid pressure reduces the crustal strength, by reducing the effective internal angle of friction (Section 2). Figure 12b illustrates a case where  $\phi_{eff} = 5^\circ$ , corresponding to significantly higher than hydrostatic fluid pressure in the upper crust. Conversely, sedimentation that buries the channel will have the opposite effect, thickening and strengthening the upper crust and therefore acting against the positive feedback that leads to channel exhumation.

When the upper crust above the channel remains stable, that is it does not extend or detach and move with the channel, the surface exhumation zone is nearly symmetric and the exhumed channel dips steeply (Fig. 12b). The boundaries of the exhumed channel record evidence of its evolution. If channel flow is not active during exhumation, the channel will have relict thrust- and normal-sense boundary layer ductile shears that were produced during the earlier phase of sub-horizontal high-temperature channel flow. Channel flow that continues during exhumation will produce additional ductile and brittle shear fabrics superimposed on the earlier ones. The near-symmetric tectonic style (Fig. 12b) is primarily the result of exhumation driven by denudation. This is less likely within a plateau because denudation is usually focused on plateau flanks. In unusual circumstances, channel exhumation may occur within a plateau where fluvial and/or glacial incision is sufficient to trigger the positive feedback mechanism.

## **6.2 Asymmetric Thrust Extrusion**

The unstable outward flow of weak upper crust together with the channel converts the near-symmetric exhumation style to asymmetric thrust extrusion, as observed in the Himalaya (Fig. 8). The upper and lower bounding shears dip at low angles (Fig. 12c) and thrust-sense shearing is enhanced by outward flow of upper crust. During this type of extrusion the upper shear zone may be normal- or thrust-sense depending on the relative velocity between the upper crust and the underlying extruding material. Most HT models of this type predict an overall cumulative normal sense of offset but this offset on the upper shear zone is less than that across the lower bounding shear.

## **6.3 Hinterland Doming by Crustal Extension**

Outward motion of the plateau upper crust during asymmetric thrust extrusion may be balanced by localized upper crustal extension within the plateau at positions ranging from near the exhumation front to above the model S-point (Fig. 7). Localized tectonic extension thins the crust, causing positive feedback between crustal thinning and channel exhumation. In this case surface denudation is unnecessary, and crustal thinning could even be accompanied by surface subsidence and sedimentation. When channel flow is efficient, the channel may inflate and balloon upward to form a dome that fills the space created by extension (Figs. 12d and 13d). In contrast, when channel flow is slower than the rate of upper crustal extension the whole crust together with the channel is uplifted isostatically without inflation, in response to the upper crustal extension.

## **6.4 Doming Triggered by Underthrusting**

Doming may also be triggered during asymmetric thrust extrusion when the leading edge of the converging, relatively strong pro-crust is injected into the mid-crustal channel. The frontal ramp underthrusts the channel, uplifts it, and squeezes it against the overlying upper crust. Given

sufficiently elevated stress, this squeezing will destabilize the upper crust and trigger extension, forming a dome above the frontal ramp (Fig. 12e). Subsequently, this dome may be translated over the ramp and toward the exhumation front. Domes created in this way lie between the suture and the denudation front. Recently formed domes of this type should be spatially correlated with the frontal ramp of the underthrust pro-crust.

### **6.5 Extruded Domes**

Rather than destabilizing the upper crust, domes formed by the underthrusting mechanism described above may be rotated, flattened, and inserted into the channel as it flows over the frontal ramp (Figs. 12f and 13f). If this process continues, deformed domes will be extruded and expelled at the denudation front. The expulsion mechanism may resemble the 'pip' mechanics proposed by *Burchfiel and Royden [1985]*, but in this case the 'pip' is initially part of the ductile channel, not strong cold crust, and it deforms as it is extruded.

### **6.6 Extrusion Zones Advected into the Plateau**

Decreasing denudation rates can lead to renewed channel tunneling in the mid-crust (Fig. 13g). In such instances, as continued convergence thickens the plateau flank, the abandoned extrusion zone becomes embedded in the newly thickened crust and is advected into the plateau (Fig. 12g).

## **7. Sensitivity of Model Results to Crustal Heterogeneity**

In all the models discussed above the crust consists of laterally uniform layers. However, in the Himalayan-Tibetan orogen, the Indian and Asian crusts are likely to have different compositions and, moreover, the earlier accretionary history [e.g., *Yin and Harrison, 2000*] may have given the Asian crust considerable internal heterogeneity. Although we have not undertaken an exhaustive sensitivity analysis to potential crustal heterogeneities, model HT-HET (Fig. 14)

provides some insight into the effect of variations in lower crustal properties on the thermal-tectonic style of the models. In particular, we focus on whether or not such variations lead to obstructions that block channel flows.

Model HT-HET is similar to model HT1 except for the properties of the lower crust, which is the strongest region of the model and, therefore, has the greatest potential to disrupt or impede channel flows. The lower pro-crust, which is not subducted (cf. type-1 models), comprises alternating 200 km wide zones with the standard dry Maryland diabase (DMD) rheology and with the same rheology but with  $B^*/10$  (DMD/10; section 2, Table 1). The strong and weak regions in the lower crust therefore have a nominal viscosity contrast of 10, which is modulated during the evolution of the model by the effect of power-law flow and temperature variations.

The results (Fig. 14) show a complexly deformed crust which can be understood in terms of two main superimposed deformation phases. The first phase activates and deforms the zones of weaker (DMD/10) lower crust. This deformation starts in the transition zone between the foreland and the plateau (Fig. 14a,b), where the horizontal pressure gradient acts in the same way as that caused by sediment prograding over salt [*Lehner, 2000*]. The weak lower crust is first squeezed and evacuated, and then thrust along with its overlying crust over adjacent strong lower crust, forming allochthonous tongues or nappes (Fig. 14a,b). The transport direction is pro-ward on the pro-side, and the converse on the retro-side. Shears at the leading edges of the nappes propagate upward through the crust, and the allochthonous nappes and their overburden evolve into shear-bounded lozenges of uplifted and transported crust. Evacuated lower crust is replaced by subsiding mid-crust, which preferentially shortens and thickens during further contraction (e.g., vertical markers - 1 to -2 and -3 to -4, Fig. 14a).

In the second phase, a channel flow develops in the heterogeneous crust created during phase one. The overthrust weak lower crustal nappes become entrained in the channel flow. The remaining zones of strong lower crust are transported into the center of the plateau and detached at S. However, instead of creating a progressively growing antiform of thickened lower crust, as in type-1 models (e.g. Fig. 3), lozenges of thickened strong lower crust are incorporated into the channel flow and are carried toward the plateau flank by the counterflow (Fig. 14). The results imply that widespread channel flows can develop even where deformation of heterogeneous lower crust leads to complex middle and lower crustal geometry and composition. If natural channels are similarly heterogeneous, they may be difficult to recognize using geophysical techniques that focus on evidence for homogeneous channels (laterally continuous reflectors and low velocity zones) and distributed melts (bright zones). Given that models with homogeneous crust are unlikely to be representative of natural crustal composition, results from models with heterogeneous lower (e.g., HT-HET, Fig. 14) and/or middle crust (not shown) may provide better analogues for lower crustal deformation in large natural orogens.

### **8. Sensitivity of Model Results to Assumed Mantle Kinematics**

All models described above have prescribed kinematic subduction and thermal conditions in the mantle. We have investigated the potential role of the sub-orogenic mantle by testing the sensitivity of the results to the assumed dip of the underthrust mantle lithosphere and to conditions that correspond to pure shear thickening of the mantle without subduction.

Varying the dip of the underthrust mantle lithosphere in type-2 models (not shown) causes small variations in the crustal temperature field, but has no significant effect on the overall tectonic character of the results. This result is not surprising because at these high convergence rates ( $\underline{V}_P + \underline{V}_R = 5$  cm/y), the temperature in the model mantle is dominated by the horizontal advection of the

mantle lithosphere, which screens the crust from the effects of deeper thermal perturbations. These results mean that little significance should be attributed to the assumed dip of subduction. The subduction zone could equally well dip in the opposite direction [cf., *Willett and Beaumont, 1994*], for example, if the subducting slab steepens and overturns as it is overridden by the retro-ward motion of the S-point.

Similarly, most of the HT1 characteristics are retained in model HT-PS (Fig. 15) in which the prescribed mantle kinematics correspond to homogeneous thickening of the mantle lithosphere in a 1000 km wide region extending for 500 km on either side of the HT1 S-point position. This pure shear type of boundary condition represents the opposite end member to subduction, which assumes no thickening of the mantle lithosphere. The lower crust is included in the dynamical part of model HT-PS, as in type-1 models, because there is no simple mechanism consistent with pure shear thickening that would allow the lower crust to be absorbed by the mantle without deformation.

The primary difference between HT1 and HT-PS is the large region of thickened lower crust that forms in the center of the orogen in HT-PS (Fig. 10 vs. Fig. 15). The thick, relatively high viscosity, lower crust inhibits the development of channel flow in the center of the model. Consequently, the upper crust and surface suture in the center of the model are not transported toward the exhumation front during denudation. In other respects, HT-PS (Fig. 15) is similar to models with subduction boundary conditions; the various tectonic styles seen in the earlier models can be reproduced by small changes in the denudation model.

These sensitivity tests demonstrate that the model characteristics in the region corresponding to southern Tibet and the Himalaya, the focus of this and the companion paper [*Jamieson et al., 2004*], are relatively insensitive to the assumed mantle kinematics below the center of the plateau.

This is not surprising because the presence of the low viscosity channel decouples the middle and upper crustal tectonics from the behavior of the lower crust and mantle [see also *Shen et al.*, 2001]. It follows that the model results should also be relatively insensitive to other mantle processes, such as break-off of the subducted continental mantle slab, provided that break-off occurs in the sub-lithospheric mantle and does not involve delamination and removal of mantle lithosphere from beneath the pro-side of the orogen. We speculate that the main effect of retro-mantle removal by convective instability or delamination will be to induce buoyant uplift in the manner proposed by *Molnar et al.* [1993] and *Platt and England* [1993]. The added buoyancy will uplift the plateau above the region subject to the convective removal or delamination and may increase the tendency for domes to form in this region. At more distant locations, such as the Himalaya and southern Tibetan plateau in the present context, the main effect may be to increase the pressure gradient in the channel and perhaps enhance channel flow. These effects can be investigated in models that include the underlying upper mantle and we anticipate reporting on these model results in the near future.

It can also be seen that the character of the crustal flow and temperature regime in HT-PS is totally different from that predicted by thin-sheet models that assume uniform thickening with depth throughout the lithosphere [e.g., *England and Houseman*, 1986]. This difference exists despite the use of a basal boundary condition that corresponds to uniform pure-shear thickening of the mantle lithosphere. The low-viscosity mid and upper crust simply decouples from the boundary condition and is driven by gravity. One consequence is the near-isothermal mid- and lower crust which allows crust at 20 km to have approximately the same temperature as the uppermost mantle. These conditions are also very different from the conductive steady state assumptions often used to

estimate lithospheric rheological stratification and corresponding strength profiles [e.g. *Ranalli*, 1987, chapter 12] and suggest caution in this approach for actively deforming large, hot orogens.

## **9. Discussion: Model Flow Modes and Tectonic Styles, with Implications for the Himalayan-Tibetan Orogen**

The model results presented above exhibit a range of tectonic styles. These can be considered to represent the superposition of one or more short-term flow modes, which are simplified velocity patterns (e.g., Poiseuille channel flow) that characterize particular flow regimes [*Beaumont et al.* 2001a, Fig. 17]. The flow modes reflect the immediate response of the system to various controls, for example the evolving crustal properties and surface denudation, and the tectonic style measures their cumulative effect. Figures 12 and 13 show specific model results that demonstrate particular tectonic styles; in Figure 16, a more conceptual interpretation of the model results is presented in terms of the flow modes, shown by vertical velocity profiles, associated with various stages of model evolution.

The tunneling mode (Fig. 16a) occurs when the denudation is too slow to influence the channel. Pro-crust from the foreland is tectonically shortened, thickened, and accreted to the plateau, which conversely grows progressively outward by advancing into the foreland. The channel tunnels outward near the edge of the plateau and the tunneling is achieved by incorporating the crust into the channel as it heats and thermally softens. This means that in the tunnelling mode the velocity near the channel tip has an outward component that includes the effect of the incorporation of new crust into the channel. When the lower crust is not converging, the velocity of flow in the channel below the plateau is parabolic, equivalent to laminar plane-Poiseuille flow for linear viscous materials [*Turcotte and Schubert*, 1982, p.234]. When the lower

crust is converging the flow develops a high-shear lower boundary layer (Fig. 16a). The crust overlying the channel is stable, i.e. it does not flow outward with the channel.

Under the plateau, away from the channel tip, the channel flow is pumped by gravity at a rate proportional to the pressure difference between the plateau and the foreland and the square of the channel thickness, and inversely proportional to the viscosity. In the transition zone between the plateau and the foreland, the horizontal flow velocity in the channel decreases as the channel narrows toward its tip, even though the pressure gradient increases with proximity to the edge of the plateau. The channel is inflated by the decelerating flow, and this effect contributes locally to crustal thickening.

In our thermal-mechanical models, the channel tip is a rheological boundary and its rate of advance in the tunneling mode is controlled by crustal temperature. In particular, the rate is determined by the lag time, approximately 20 My, for heating of tectonically thickened crust, and corresponding decrease in viscosity, to the point that the channel can be propagated by the available pressure gradient [*Medvedev and Beaumont, 2001; in prep.*]. This approach contrasts with that of *Clark and Royden [2000]*, who addressed injection into an existing channel flanking the plateau without considering the thermal evolution of the system or the change in channel characteristics across the plateau edge. It seems unlikely that a suitably prepared channel region, with sufficiently low viscosities for injection, will exist in normal crust or crust that has recently been tectonically thickened. For this reason we suggest that channel flows will normally be thermally limited at the boundaries of plateaus [*Medvedev and Beaumont, 2001; in prep.*].

The tunneling mode shown in Figure 16a may be a reasonable approximation to the Himalayan tectonic style prior to significant exhumation of the channel. This is also inferred to be the current style of parts of the eastern margin of the Tibetan plateau [*Royden et al., 1997; Wang et*

*al.*, 1998; *Chen et al.*, 2000; *Clark and Royden*, 2000; *Kirby et al.*, 2000, 2003] except that the lower crust may be stationary or moving slowly eastward as part of the South China block [*Holt*, 2000; *Wang et al.*, 2001].

The model response to efficient denudation of the plateau flank is to raise the channel progressively toward the surface in a near-symmetric exhumation mode (Fig. 16b). Once the channel is exposed, channel flow *per se* may or may not be active. Active extrusion of channel material (e.g., Fig. 16b) will only occur if the channel flow breaks through to the surface. In the models, this is determined by the upper crustal properties, frictional strength, and degree of advective thinning of the surface boundary layer. Conceptually, a threshold exhumation rate must be achieved to keep the channel sufficiently hot so that the material does not 'freeze' until it is close to the surface. This situation may have been achieved in the Nanga Parbat - Hormuz massif [*Craw et al.*, 1994; *Zeitler et al.*, 2001; *Koons et al.*, 2002]. In nature, crustal fluid pressures and strain-dependent rock properties that lead to strain localization will also determine whether the channel remains open. A limitation of the current models, which do not include strain localization, is that the threshold exhumation rate for extrusion is probably too high, requiring denudation rates of 1 cm/y or more for surface extrusion as shown in Fig. 16b. A related Himalayan problem is whether the currently exposed GHS more closely resembles an exhumed plugged channel, with little extrusion during exhumation, or whether there was (and perhaps still is) active extrusion at the surface [*Hodges et al.* 2001; *Wobus et al.*, 2003] like a very sluggish salt fountain [*Talbot et al.*, 2000].

If efficient denudation exhumes the channel and allows active extrusion, inefficient denudation causes crustal shortening and thickening to be focused at the plateau flank. This creates antiforms, crustal-scale folds and plug-like structures, and focused thrust-sense shear zones

adjacent to the end of the channel (Fig. 16c). Under these circumstances the channel is not exhumed. Instead, the pro-crust is tectonically thickened and then exhumed in similar way to the behavior of denuding pro- and retro-wedges in small, cold orogens [Willett *et al.*, 1993; Willett, 1999].

If the crustal overburden above the channel becomes unstable, the channel flow regime may convert to Couette flow and the overburden will flow outward with a uniform velocity with depth above the channel (Fig. 16d). The Couette flow velocity in the channel decreases linearly with depth when the horizontal pressure gradient is negligible, or has a superimposed parabolic, Poiseuille, component when forced by the pressure pumping. This flow mode is facilitated by efficient flank denudation and exhumation of the channel, which help to create a 'free' outer end to the upper crust above the channel. The upper crust may then glide under gravity or be dragged by the underlying channel flow. Outward-moving upper crust then overrides the exhumed channel and converts the geometry of the exhumation zone from the near-symmetric mode (Fig. 16b) to the asymmetric thrust exhumation/extrusion mode (Fig. 16d). Creation of conditions leading to upper crustal instability requires efficient denudation, which implies that the flow mode should normally progress from the steeply dipping channel (Fig. 16b) to the moderate dips typical of the Himalaya (Fig. 8b). Intermediate tectonic styles are also possible, and in some cases the crustal overburden may move faster than the channel material.

Superimposed flow modes will be recorded by superimposed phases of finite shear of the boundary layer between the channel and the overburden. For example, in a system that evolves through the stages illustrated in Figures 16a, b, and d, the boundary layer between the channel and overburden, corresponding to the STD zone in the Himalaya, should record early normal-sense shear, followed by features indicating reduced strain rates, quiescence, or even thrust-sense shear.

In contrast, the base of the channel, corresponding to the MCT zone, should record protracted thrust-sense shear.

If the stability of the crustal overburden varies laterally, the intervening region will deform, most likely by extension (Fig. 16e). Upper crustal extension and thinning will result in doming of the channel and its overburden (Fig. 16e) if the characteristic timescale for channel flow into the extending region is less than the timescale for extension. Under these circumstances, the channel material behaves as a fluid and is pumped into the region of relatively low pressure caused by crustal extension and thinning (Fig. 16e). Similar behavior has been inferred to occur in the footwalls beneath extensional metamorphic core complexes [e.g., *Wernicke, 1990; Block and Royden, 1990; Kruse et al., 1991*], and domes created in this way (Fig. 16e) could be interpreted as core complexes.

Continued convergence after exhumation of the channel can trigger additional tectonic effects (Fig. 16f,g) related to underthrusting by converging middle and lower pro-crust. A fundamental change in flow mode and corresponding tectonic regime would result if outward channel growth by tunneling is replaced by channel contraction as it is underthrust and squeezed by the converging crust. A mode change of this type in the Himalayan-Tibet system would represent an event that punctuates the otherwise progressive evolution of the system through the flow modes illustrated in Figure 16 (a,b,d). When the channel is deflected upward during exhumation (e.g. Fig. 16b,d) it may cease to tunnel through the mid-crust. If convergence continues, relatively cold, strong pro-mid crust inserts itself into the channel, forming a ramp-flat geometry at its leading edge (Fig. 16f) that is inherited from the footwall geometry of the channel beneath the exhumation zone (e.g. Fig. 16b). Squeezing of the channel above the ramp can destabilize the upper crustal overburden, triggering the formation of a dome (Fig. 16f). This may provide a possible explanation for the formation of

the belt of gneiss domes, including the Kangmar [Lee *et al.*, 2000] and Mabja domes [Lee *et al.*, 2001], associated with the north Himalayan antiform and interpreted by Hauck *et al.* [1998] to be above a ramp in the Main Himalayan Thrust (Fig. 8b). Domes of this type are initially formed above the crustal ramp, but with additional convergence they will be transported relatively pro-ward, toward the plateau flank. This process can trigger an isolated dome in the plateau (cf. Fig. 16e,f), or smaller domes with less structural relief can be expelled/extruded along the channel like a deforming egg in a snake (Fig. 16g), eventually emerging at the surface. Structural domes reported from some GHS localities [e.g., Zaskar-Lahul region, Stephenson *et al.*, 2000; Walker *et al.*, 2001; Robyr and Steck, 2001] may represent features formed beneath the southern Tibetan plateau and then extruded in this manner.

An analogous model involving crustal injection and hydraulic uplift was proposed by Zhao and Morgan [1987]. In this case only crust was injected [Fig. 1 of Zhao and Morgan, 1987] and the resulting hydraulic pumping effect of the crustal plunger was proposed as a mechanism for the uplift of Tibet. In the present models, the inserted crust remains attached to underlying lower crust and mantle and the process occurs during overall lithospheric convergence. Our current model results suggest that the plateau would be tectonically unstable during uplift by hydraulic pumping, leading to extension and doming that would prevent this mechanism causing a general increase in the elevation of the Tibetan plateau. In other respects the Zhao and Morgan (1987) results and our results are quite similar, with our models illustrating how the proposed configuration of their model may have developed.

## 10. Conclusions

Results have been presented for a range of plane-strain thermal-mechanical finite element models of collisional orogenesis in large hot orogens. The purpose is to investigate the styles of

deformation as radioactive self-heating progressively reduces the viscosity of the crust following tectonic thickening, and increases its susceptibility to large scale horizontal flow. Under certain conditions the models develop mid-crustal channel flows driven by differential pressure, and the channel material tunnels outward in the mid-crust from beneath the model plateau toward its flanks. The channel may be exhumed and exposed at the surface by climatically enhanced surface denudation focused on the steep, high-relief transition region between the plateau and the foreland.

Generic type-1 models, used to test the model sensitivity to the denudation and the choice of effective viscosity of the channel, demonstrate that channel flows do not develop, or are sluggish, if the mid and upper crust has a ductile rheology based on the wet-quartzite flow law of Gleason and Tullis (1995). However, further reduction of the effective viscosity to  $10^{19}$  Pa.s or less leads to well-developed channel flows and we interpret this additional decrease to the effect of a small *in situ* component of partial melt. This effect is included in the models by empirical crustal 'melt-weakening' at temperatures between  $700^{\circ}$  and  $750^{\circ}\text{C}$  corresponding to muscovite dehydration melting. We therefore conclude that crustal anatexis and the development of a migmatitic mid-crust will promote channel flows. However, *in situ* melt is not required if other processes reduce the effective viscosity to the same degree over the same temperature range.

Models in which the effective viscosity was reduced to  $2 \times 10^{18}$  Pa.s do not show the corresponding factor of five increase in channel flow velocity predicted by the simple theory for infinitely long channels. This is because the channel flow regime is limited by the low temperature, high viscosity crust in the transition region between the plateau and foreland. The rate at which the channel tip tunnels outward is determined by the same restriction, the lag time, approximately 20 My, for tectonically thickened crust to heat sufficiently and for the viscosity to decrease sufficiently so that the mid-crust will participate in the channel flow.

Type-2 models were designed for comparison with a representative north-south cross section of the Himalayan-Tibetan orogen. In Model HT1, the channel is erosionally exhumed to the surface, and this exhumation also leads to instability of the upper crust and its outward flow together with the channel. This model (Fig. 10) is in broad agreement with many Himalayan observations (Fig. 17) and it provides an internally consistent explanation for the dynamical behavior of the Himalaya as a system. Partially molten Indian crust tunneled outward beneath the Tibetan plateau and was exhumed to the surface by rapid erosion of the southern flank of the Himalaya (1) (numbers refer to Fig. 17). The channel material was extruded between the coeval MCT and STD ductile shear systems (2 and 3), thereby accounting for their opposite shear sense, and exposed as the high grade, migmatitic GHS (4). Equivalent partially molten crust continues to exist beneath Tibet (5) and further diachronous erosion may expose this crust as a future GHS. The contrast in protoliths across the MCT system (6) results from tectonic juxtaposition of the extruded GHS, which is derived from crust that entered the orogen early in its evolution, and the recently accreted LHS which is derived from crust located up to 1000 km further to the south. The model also accounts for the 'inverted' metamorphism of the MCT and LHS zones (7) and is compatible with a range of P-T and geochronological data [Jamieson *et al.*, 2004]. The position of the Indus-Tsangpo suture (8) is replicated by the model, but this result is non-unique because it depends on the tradeoff between the total amount of crust eroded from the Himalayan flank of the model and the total northward advance in the subduction point in the basal boundary condition.

A sensitivity analysis of model behavior indicates that a single or unique Himalayan tectonic style is unlikely. Several flow modes (Fig. 16) are recognized and lead to differing tectonic styles (Figs. 12 and 13). That relatively small differences in denudation rates and crustal properties lead to this range of tectonic styles suggests that the Himalayan system will also exhibit an

equivalent range of styles because variations in denudation rates and crustal properties will certainly exist along the length of the Himalayan front [see *Jamieson et al.*, 2004 Section 10.4]. Flow modes that cause extension of the upper crust can lead to the development of domes that resemble at least some of the north Himalayan gneiss domes ( Fig. 17, (9)). In particular, the Kangmar dome is interpreted to be a dome triggered by underthrusting of a ramp in the MHT (10).

Preliminary tests indicate that channel flows will operate in the models even when zones of stronger, not melt-weakened, lower crust become entrained in the channel and cause it to become heterogeneous. Equivalent heterogeneous natural channels may prove difficult to recognize geophysically.

Tests of the model sensitivity to the choice of kinematic basal boundary conditions indicate that the overall tectonic regime, and, in particular the channel flow, remain similar even under boundary conditions that correspond to regional uniform thickening of the mantle lithosphere beneath the center of the model. This is not surprising because the weak channel decouples the crust from motion of the lower crust and mantle on all but the largest orogen scales. It also follows that deformation and temperature regimes in models with channel flows will be completely different from those predicted by 'thin sheet' models which require velocities to be constant with depth through the lithosphere. This is because models with channels behave as three weakly coupled layers whereas 'thin sheet' models are constrained to act as a single layer.

### **Acknowledgements**

This work is dedicated to the memory of Doug Nelson, who challenged us to produce model results compatible with observations from the Himalayan-Tibetan orogen. The research was funded by Natural Sciences and Engineering Research Council and Lithoprobe Supporting Geoscience grants to CB and RAJ. CB has also been supported by the Inco Fellowship of the Canadian Institute

for Advanced Research, and by the Canada Research Chairs program. The models were developed and run with the assistance of Phillippe Fullsack and Bonny Lee. The work has benefited greatly from discussions with many colleagues, including Doug Nelson, Djordje Grujic, and Yani Najman and members of the CIAR-ESEP. We thank the reviewers, Greg Housman and Joseph Martinod, and the associate editor, Jean Braun, for their constructive comments.

## References

- Beaumont, C., R.A. Jamieson, M.H. Nguyen, and B. Lee, Mid-crustal channel flow in large hot orogens: results from coupled thermal-mechanical models, in *Slave - Northern Cordillera Lithospheric Evolution (SNORCLE) and Cordilleran Tectonics Workshop; Report of 2001 Combined Meeting, Lithoprobe Report*, compiled by F. Cook and P. Erdmer, pp. 112-170, 2001a.
- Beaumont, C., R.A. Jamieson, M.H. Nguyen, and B. Lee, Himalayan tectonics explained by extrusion of a low-viscosity channel coupled to focused surface denudation, *Nature*, *414*, 738-742, 2001b.
- Bird, P., Initiation of intracontinental subduction in the Himalaya, *Journal of Geophysical Research*, *83*, 4975-4987, 1978.
- Bird, P., Lateral extrusion of lower crust from under high topography, in the isostatic limit, *Journal of Geophysical Research*, *96*, 10275-10286, 1991.
- Block, L., and L.H. Royden, Core complex geometries and regional scale flow in the lower crust, *Tectonics*, *9*, 557-567, 1990.
- Burchfiel, B.C., and L.H. Royden, North-south extension within the convergent Himalayan region, *Geology*, *13*, 679-682, 1985.
- Chen, Z., B.C. Burchfiel, Y. Liu, R.W. King, L.H. Royden, W. Tang, E. Wang, J. Zhao, and X. Zhang, Global positioning system measurements from eastern Tibet and their implications for India/Eurasia intercontinental deformation, *Journal of Geophysical Research*, *105*, 16215-16227, 2000.
- Clark, M.K., and L.H. Royden, Topographic ooze: Building the eastern margin of Tibet by lower crustal flow, *Geology*, *28*, 703-706, 2000.
- Craw, D., P.O. Koons, D. Winslow, C.P. Chamberlain, and P. Zeitler, Boiling fluids in a region of rapid uplift, Nanga Parbat massif, Pakistan, *Earth and Planetary Science Letters*, *128*, 169-182, 1994.

- DeCelles, P.G., D.M. Robinson, and G. Zandt, Implications of shortening in the Himalayan fold-thrust belt for uplift of the Tibetan Plateau, *Tectonics*, 21 (1062), doi:10.1029/2001TC001322, 2002.
- Dewey, J.F., R.M. Shackleton, C. Chang, and Y. Sun, The tectonic evolution of the Tibetan plateau, *Philos. Trans. R. Soc. London, A*, 327, 379-413, 1988.
- England, P., and Houseman, G., Finite strain calculations of continental deformation 2. Comparison with the India-Asia Collision zone, *Journal of Geophysical Research*, 91, 3664-3676, 1986.
- Fullsack, P., An arbitrary Lagrangian-Eulerian formulation for creeping flows and its application in tectonic models, *Geophysical Journal International*, 120, 1-23, 1995.
- Gleason, G.C., and J. Tullis, A flow law for dislocation creep of quartz aggregates determined with the molten salt cell, *Tectonophysics*, 247, 1-23, 1995.
- Grujic, D., M. Casey, C. Davidson, L.S. Hollister, R. Kundig, T. Pavlis, and S. Schmid, Ductile extrusion of the Higher Himalayan Crystalline in Bhutan: Evidence from quartz microfabrics, *Tectonophysics*, 260, 21-43, 1996.
- Haines, S.S., S.L. Klemperer, L. Brown, J. Guo, J. Mechie, R. Meissner, A. Ross, and W. Zhao, INDEPTH III seismic data: From surface observations to deep crustal processes in Tibet, *Tectonics*, 22 (1001), doi:10.1029/2001TC001305, 2003.
- Hauck, M.L., K.D. Nelson, L.D. Brown, W. Zhao, and A.R. Ross, Crustal structure of the Himalayan orogen at ~90° east longitude from Project INDEPTH deep reflection profiles, *Tectonics*, 17, 481-500, 1998.
- Hodges, K.V., Tectonics of the Himalaya and southern Tibet from two perspectives, *Geological Society of America Bulletin*, 112, 324-350, 2000.
- Hodges, K.V., J.M. Hurtado, and K.X. Whipple, Southward extrusion of Tibetan crust and its effect on Himalayan tectonics, *Tectonics*, 20, 799-809, 2001.
- Holt, W.E., Correlated crust and mantle strain fields in Tibet, *Geology*, 28, 67-70, 2000.
- Houseman, G.A., D.P. McKenzie, and P. Molnar, Convective instability of a thickened boundary layer and its relevance for the thermal evolution of continental convergent belts, *Journal of Geophysical Research*, 86, 6115-6132, 1981.
- Jamieson, R.A., C. Beaumont, M.H. Nguyen, and B. Lee, Interaction of metamorphism, deformation, and exhumation in large convergent orogens, *Journal of Metamorphic Geology*, 20, 1-16, 2002.

- Jamieson, R.A., C. Beaumont, S. Medvedev and M.H. Nguyen, Crustal channel flows: 2. Numerical models with implications for metamorphism in the Himalayan-Tibetan Orogen, *Journal of Geophysical Research*, in this volume, 2004.
- Johnson, M.R.W., Shortening budgets and the role of continental subduction during the India-Asia collision, *Earth Science Reviews*, 59, 101-123, 2002.
- Kirby, E., K.X. Whipple, B.C. Burchfiel, W. Tang, G. Berger, Z. Sun, and Z. Chen, Neotectonics of the Min Shan, China: Implications for mechanisms driving Quaternary deformation along the eastern margin of the Tibetan Plateau, *Geological Society of America Bulletin*, 112, 375-393, 2000.
- Kirby, E., K.X. Whipple, W. Tang, and Z. Chen, Distribution of active rock uplift along the eastern margin of the Tibetan Plateau: Inferences from bedrock channel longitudinal profiles, *Journal of Geophysical Research*, 108 (B4) (2217), doi:10.1029/2001JB000861, 2003.
- Koons, P.O., P.K. Zeitler, C.P. Chamberlain, D. Craw, and A.S. Meltzer, Mechanical links between erosion and metamorphism in Nanga Parbat, Pakistan Himalaya, *American Journal of Science*, 302, 749-773, 2002.
- Kruse, S., M. McNutt, J. Phipps-Morgan, L. Royden, and B. Wernicke, Lithospheric extension near Lake Mead, Nevada: A model for ductile flow in the lower crust, *Journal of Geophysical Research*, 96, 4435-4456, 1991.
- Le Pichon, X., M. Fournier, and L. Jolivet, Kinematics, topography, shortening, and extrusion in the India-Eurasia collision, *Tectonics*, 11, 1085-1098, 1992.
- Lee, J., B.R. Hacker, W.S. Dinklage, Y. Wang, P. Gans, A. Calvert, J.L. Wan, W. Chen, A.E. Blythe, and W. McLelland, Evolution of the Kangmar Dome, southern Tibet: Structural, petrologic, and thermochronologic constraints, *Tectonics*, 19, 872-895, 2000.
- Lee, J., Y. Wang, M. McWilliams, J. Hourigan, A. Blythe, and W. McClelland, Cooling history in Mabja dome, southern Tibet: Implications for the tectonic evolution of the north Himalayan gneiss domes, *Eos Transactions of the American Geophysical Union*, 82, Fall Meet. Suppl., Abstract T11E-0889, 2001.
- Lehner, F.K., Approximate theory of substratum creep and associated overburden deformation in salt basins and deltas, in *Aspects of Tectonic Faulting: In Honour of Georg Mandl*, edited by F.K. Lehner, and J.L. Urai, pp. 21-47, Springer-Verlag Telos, 2000.
- Mackwell, S.J., M.E. Zimmerman, and D.L. Kohlstedt, High-temperature deformation of dry diabase with application to tectonics on Venus, *Journal of Geophysical Research*, 103, 975-984, 1998.
- Mahéo, G., S. Guillot, J. Blichert-Toft, Y. Rolland, and A. Pêcher, A slab breakoff model for the Neogene thermal evolution of South Karakoram and South Tibet, *Earth and Planetary Science*

*Letters*, 195, 15-58, 2002.

- Medvedev, S., and C. Beaumont, Models for Mid and Lower Crustal Channel Flows, *Eos Transactions of the American Geophysical Union*, 82 (47), Fall Meet. Suppl., Abstract T12D-0937, 2001.
- Medvedev, S. and C. Beaumont, Growth of continental plateaux: Channel injection or tectonic thickening? in preparation for *Journal of Geophysical Research*.
- Molnar, P., P. England, and J. Martinod, Mantle dynamics, uplift of the Tibetan plateau, and the Indian monsoon, *Reviews of Geophysics*, 31, 357-396, 1993.
- Myrow, P.M., N.C. Hughes, T.S. Paulsen, I.S. Williams, S.K. Parcha, K.R. Thompson, S.A. Bowring, S.-C. Peng, and A.D. Ahluwalia, Integrated tectonostratigraphic analysis of the Himalaya and implications for its tectonic reconstruction, *Earth and Planetary Science Letters*, 212, 433-441, 2003.
- Owens, T.J., and G. Zandt, Implications of crustal property variations for models of Tibetan plateau evolution, *Nature*, 387, 37-43, 1997.
- Platt, J.P., and P.C. England, Convective removal of lithosphere beneath mountain belts: Thermal and mechanical consequences, *American Journal of Science*, 293, 307-336, 1993.
- Pope, D.C., and S.D. Willett, Thermal-mechanical model for crustal thickening in the Central Andes driven by ablative subduction, *Geology*, 26, 511-514, 1998.
- Ranalli, G., *Rheology of the Earth*, 366 pp., Allen and Unwin, Winchester Mass., 1987.
- Robyr, M. and A. Steck, Thrusting, extension, and doming during the polyphase tectono-metamorphic evolution of the High Himalayan Crystalline Sequence in SE Zaskar and NW Lahul, *Journal of Asian Earth Sciences*, 19, 52-54, 2001.
- Rowley, D.B., Cenozoic paleoaltimetry and paleohypsometry of the Himalaya and Tibet plateau., *Geological Association of Canada, Abstracts with programs*, 34 (6), 472, 2002.
- Royden, L.H., The steady-state thermal structure of eroding orogenic belts and accretionary prisms, *Journal of Geophysical Research*, 98, 4487-4507, 1993.
- Royden, L.H., Coupling and decoupling of crust and mantle in convergent orogens: Implications for strain partitioning in the crust, *Journal of Geophysical Research*, 101, 17679-17705, 1996.
- Royden, L.H., B.C. Burchfiel, R.W. King, Z. Chen, F. Shen, and Y. Liu, Surface deformation and lower crustal flow in eastern Tibet, *Science*, 276, 788-790, 1997.
- Searle, M.P., Cooling history, erosion, exhumation, and kinematics of the Himalaya-Harakoram-Tibet orogenic belt, in *Tectonics of Asia*, edited by A. Yin and T.M. Harrison, pp. 110-137,

Cambridge University Press, 1996.

Shen, F., L.H. Royden, and B.C. Burchfiel, Large-scale crustal deformation of the Tibetan Plateau, *Journal of Geophysical Research*, 106, 6793-6816, 2001.

Spicer, R., N. Harris, M. Widdowson, A. Herman, S. Guo, P. Valdes, J. Wolfe, and S. Kelley, Constant elevation of southern Tibet over the past 15 million years, *Nature*, 421, 622-624, 2003.

Stephenson, B.J., D.J. Waters, and M.P. Searle, Inverted metamorphism and the Main Central Thrust: Field relations and thermobarometric constraints from the Kishtar Window, NW Indian Himalaya, *Journal of Metamorphic Geology*, 18, 571-590, 2000.

Talbot, C.J., S. Medvedev, M. Alavi, H. Shahrivar, and E. Heidari, Salt extrusion at Kuh-e-Jahani, Iran, from June 1994 to November 1997, in *Salt, Shale, and Igneous Diapirs in and around Europe*, edited by Vendeville B. et al., pp. 93-110, *Geological Society Special Publication*, 174, 2000.

Tao, W.C., and R.J. O'Connell, Ablative subduction: A two-sided alternative to the conventional subduction model, *Journal of Geophysical Research*, 97, 8877-8904, 1992.

Tilmann, F., J. Ni, and INDEPTH III Seismic Team, Seismic imaging of the downwelling Indian lithosphere beneath central Tibet, *Science*, 300, 1424-1427, 2003.

Turcotte, D.L., and G. Schubert, *Geodynamics: Applications of Continuum Physics to Geological Problems*, 450 pp., John Wiley & Sons, 1982.

van der Voo, R., W. Spakman, and H. Bijwaard, Tethyan subducted slabs under India, *Earth and Planetary Science Letters*, 171, 7-20, 1999.

Vanderhaeghe, O., C. Beaumont, P. Fullsack, S. Medvedev, and R.A. Jamieson, Thermal-mechanical modeling of convergent orogens: The role of rheology, isostasy, and temperature, in *Eastern Canadian Shield Onshore-Offshore Transect (ECSOOT): Report of 1999 Transect Meeting*, compiled by J. Hall, and R.W., pp. 44-84, *Lithoprobe Report*, 73, 1999.

Vanderhaeghe, O., S. Medvedev, P. Fullsack, C. Beaumont, and R.A. Jamieson, Evolution of orogenic wedges and continental plateaux: Insights from crustal thermal-mechanical models overlying subducting mantle lithosphere, *Geophysical Journal International*, 153, 27-51, 2003.

Vannay, J.-C., and B. Grasemann, Himalayan inverted metamorphism and syn-convergence extension as a consequence of a general shear extrusion, *Geological Magazine*, 138, 253-276, 2001.

Walker, C.B., M.P. Searle, and D.J. Waters, An integrated tectonothermal model for the evolution of the High Himalaya in western Zaskar with constraints from thermobarometry and metamorphic modeling, *Tectonics*, 20, 810-833, 2001.

- Wang, E., B.C. Burchfiel, L.H. Royden, L. Chen, J. Chen, W. Li, and Z. Chen, Late Cenozoic Xianshuihe-Xiaojiang and Red River fault systems of southwestern Sichuan and central Yunnan, China, *Geological Society of America, Special Paper*, 327, 108 pp., 1998.
- Wang, Q., P.Z. Zhang, J.T. Freymueller, R. Bilham, K.M. Larson, X. Lai, X. You, Z. Niu, J. Wu, Y. Li, J. Liu, Z. Yang, and Q. Chen, Present-day crustal deformation in China constrained by global positioning system measurements, *Science*, 294, 574-577, 2001.
- Waschbusch, P., and C. Beaumont, Effect of a retreating subduction zone on deformation in simple regions of plate convergence, *Journal of Geophysical Research*, 101, 28133-28148, 1996.
- Wernicke, B., The fluid crustal layer and its implications for continental dynamics, in *Exposed cross-sections of the continental crust*, edited by M.H. Salisbury, and D.M. Fountain, pp. 509-544, Kluwer, Norwell, Mass., 1990.
- Westaway, R., Crustal volume balance during the India-Eurasia collision and altitude of the Tibetan plateau: A working hypothesis, *Journal of Geophysical Research*, 100, 15173-15192, 1995.
- Willett, S.D., C. Beaumont, and P. Fullsack, Mechanical model for the tectonics of doubly vergent compressional orogens, *Geology*, 21, 371-374, 1993.
- Willett, S.D., and C. Beaumont, Subduction of Asian lithospheric mantle beneath Tibet inferred from models of continental collision, *Nature*, 369, 642-645, 1994.
- Willett, S.D., Orogeny and orography: The effects of erosion on the structure of mountain belts, *Journal of Geophysical Research*, 104, 28957-28981, 1999.
- Wobus, C.W., K.V. Hodges, and K.X. Whipple, Has focused denudation sustained active thrusting at the Himalayan topographic front? *Geology*, 31, 861-864, 2003
- Yin, A., and T.M. Harrison, Geologic evolution of the Himalayan-Tibetan Orogen, *Annu. Rev. Earth Planet. Sci.*, 28, 211-180, 2000.
- Zeitler, P.K., A.S. Meltzer, P.O. Koons, D. Craw, B. Hallet, C.P. Chamberlain, W.S.F. Kidd, S.K. Park, L. Seeber, M. Bishop, and J. Shroder, Erosion, Himalayan geodynamics, and the geomorphology of metamorphism, *GSA Today*, 11, 4-9, 2001.
- Zhao, W.L., and W.J. Morgan, Injection of Indian crust into Tibetan lower crust: A two dimensional finite element model study, *Tectonics*, 6, 489-504, 1987.

## Figure Captions

**Figure 1.** Initial conditions, Model 1. Other type-1 models are similar but have different melt weakening and denudation parameter values (Table 1), and Model 5 includes a weak, 10 km thick, upper crust. Type-2 models are similar to Model 5 but have advancing subduction boundary conditions (see section 4 and *Jamieson et al.*, [2004], Figure 1). Only the central region of the model is shown here; full model width is 2000 km. a) Passive marker grid and mechanical layers (light grey = mid and upper crustal layer, details in c). Vertical markers numbered to facilitate comparison with deformed grids (e.g. Fig. 3); '0' = model suture above subduction point, S. b) Initial thermal structure, radioactive layers,  $A_1$  and  $A_2$  (see panel c), initial isotherms (horizontal lines) calculated for conductive steady state with  $T_s = 0^\circ\text{C}$  and  $q_m = 20\text{mW/m}^2$ , and instantaneous velocity vectors (short dark lines). Velocities  $V_P = 2\text{ cm/y}$  and  $V_S = V_R = 0$  specified kinematically in mantle lithosphere and determined dynamically in crust. Surface denudation rate given by the product of local surface slope,  $f(t)$  and  $g(x)$ ; functions defined in Table 1. c) Relationship between initial mechanical and thermal layers and summary of parameters (see also Table 1). d) Effect of reduction in viscosity from flow law value at  $700^\circ\text{C}$  to  $10^{19}\text{ Pa.s}$  at  $750^\circ\text{C}$  ('melt weakening'). Effective viscosity used in model shown by solid line, that predicted by flow law(s) shown schematically by dashed line. Further details in text and Table 1.

**Figure 2.** Crustal-scale deformation and thermal evolution of Model 1 for 30 My of the set-up phase during which there is no surface denudation ( $V=H$ ). Upper panel in each set shows deformed marker grid and mechanical layers (grey = mid and upper crustal layer); lower panel shows isotherms (contoured at  $100^\circ\text{C}$  intervals), velocity vectors, and thermal layers (grey =  $A_1$  layer).

Heavy line with dots represents position of model suture (below vertical marker '0'). Panels a-d show stages in the evolution for time,  $t$ , and convergence  $\Delta x$ .

**Figure 3.** Crustal-scale deformation and thermal evolution of Model 1 between 45 and 60 My (V=H). Upper and lower panels in each set correspond to those described in Figure 1. Also shown in upper panels is the distribution and rate of slope-dependent erosion across the model surface; scale maximum = 1 cm/y. Panels a-c show stages in the evolution for time,  $t$  and convergence  $\Delta x$ . Panel d shows the retro-side of the model at 60 My.

**Figure 4.** Evolution of the topography for Model 1 shown with respect to the S-point,  $x = 0$  (Fig. 1). The height scale is shown for two representative isostatic balances which depend on  $\Phi = \Delta\rho / \rho_m$ , where  $\Delta\rho = \rho_m - \rho_c$  and  $\rho_m$  and  $\rho_c$  are the mantle and crust densities, respectively. The scale of the height is most sensitive to  $\Delta\rho$  and the results are therefore shown for  $\Delta\rho = 500$  and  $600 \text{ kg/m}^3$ , corresponding to  $\Phi = 0.156$  and  $0.182$ , respectively.

**Figure 5.** Upper panels; crustal-scale deformation and thermal evolution of Model 1 at  $t = 75$  My, convergence  $\Delta x = 1500$  km shown as in Figures 1 and 2 (V=H). Lower panels; total and decomposed velocity distributions (vectors, short dark lines). See text for explanation.

**Figure 6.** Crustal-scale deformation and thermal evolution of Models 2-4 at 75 My (panels a-c) shown as in Figures 1 and 2. Models are variations on Model 1 (Table 1). c) Also shows the total and decomposed velocity distributions at 75 My (vectors, short dark lines). See text for explanation.

**Figure 7.** Crustal-scale deformation and thermal evolution of Model 5 at 75 My shown as in Figures 1 and 2 except weak upper crustal layer (Table 1) is white. Lower panels show the total and decomposed velocity distributions (vectors, short dark lines) for comparison with Model 1 (Fig. 5).

**Figure 8.** Representative north-south cross sections of the Himalayan-Tibetan orogen. a)

Lithosphere scale section modified from *Owens and Zandt* [1997] using information compiled by *DeCelles et al.* [2002) and from *Johnson* [2002], *Tillmann et al.* [2003], and *Haines et al.* [2003].

b) Crust and uppermost mantle scale section showing Himalaya and southern Tibet, modified from *Nelson et al.* [1996] using information from *Hauck et al.* [1998], and *DeCelles et al.* [2002].

Numbers denote problems and processes considered fundamental to a comprehensive model of the orogen [*Hodges, 2000*], including: (1) rapid erosion of the southern flank of the Himalaya; (2) shortening on the Main Central Thrust (MCT) system and thrust faults to the south; (3) extension on the South Tibetan Detachment (STD) system; (4) high-grade metamorphism and anatexis in the Greater Himalayan Sequence (GHS); (5) melting in the middle crust beneath Tibet; (6) juxtaposition of contrasting protoliths across the MCT zone; (7) 'inverted' metamorphism within the MCT zone and subjacent Lesser Himalayan sequence; (8) the position of the Indus-Tsangpo suture, and; (9) north-south extension in the southern Tibetan plateau.

**Figure 9.** Explanation of model boundary conditions. In each panel pro- and retro-crusts (India and Asia) are respectively grey and black. S marks the subduction point (mantle suture) and Su the corresponding surface suture. Basal velocities are shown by arrows and labeled  $V_P$ ,  $V_S$  and  $V_R$  in the Asia fixed reference frame. a) Boundary conditions for Model 1 with  $V_P = 2$  cm/y and  $V_S = V_R = 0$

and no subduction of the lower crust. b) Corresponding boundary conditions for the Himalayan-Tibetan orogen, again with no lower crustal subduction. c) Boundary conditions and progressive evolution of Model HT1, with lower crustal subduction, showing the effect of advancing subduction on the position of S and distributions of Indian and Asian crusts in the Asia fixed reference frame. For reference, in this model a Tethyan oceanic slab that detached at the onset of collision and remained stationary in the mantle would now be located below S ( $t = 0$  My panel), a distance  $\Delta x = 1350$  km south of the current position of S ( $t = 54$  My panel). Note model results in subsequent figures are shown in a fixed S reference frame.

**Figure 10.** Crustal-scale deformation and thermal evolution of model HT1 ( $V=H$ ) [see also Figure 2, *Jamieson et al.*, 2004]. Upper panel in each set shows deformed marker grid and mechanical layers (grey = mid crustal layer); lower panel shows isotherms, velocity vectors, and thermal layers (grey =  $A_1$  layer). Heavy line with dots represents position of model suture (vertical marker '0'). Also shown is the distribution and rate of slope-dependent erosion across the model surface, scale maximum = 1 cm/y. a-d show the 30-54 My evolution during which overall convergence,  $\Delta x$ , increases from 1500 to 2700 km. Note the migration of the surface suture, '0', with respect to the mantle suture, S, and the 'Himalayan' denudation front. For ease of display the results are shown in the fixed S point reference frame thereby avoiding an excessively wide figure (cf. equivalent to Fig. 9 panels c). Transformation into the Asia fixed frame offsets successively lower panels further to the right so that the S point would be positioned at  $\Delta x = 750, 975, 1200,$  and  $1350$  km, respectively, as shown on the figure. Animations at [http://geodynam.ocean.dal.ca/jgr/test54\\_1.gif](http://geodynam.ocean.dal.ca/jgr/test54_1.gif) and [http://geodynam.ocean.dal.ca/jgr/test54\\_2.gif](http://geodynam.ocean.dal.ca/jgr/test54_2.gif)

**Figure 11.** Evolution of the topography for model HT1 shown in the fixed S-point reference frame in the same manner as Figure 10. The height is shown for the same representative isostatic balances as those shown for Model 1 in Figure 4.

**Figure 12.** Crustal-scale deformation shown for a region corresponding to the Himalaya and southern Tibet for a series of models that exhibit differing tectonic styles in response to variations in denudation rate and upper crustal strength (shown in white) ( $V=H$ ). All models have the same advancing subduction boundary conditions as HT1. They differ from HT1 in regard to maximum denudation rate; labeled H = high ( $>1.4$  cm/y), M = moderate (0.4-1.4 cm/y) and L = low ( $<0.4$  cm/y) on panels a-g. They also differ from HT1 in regard to upper crustal frictional properties (labeled as 5 and  $15^\circ$ , the effective internal angle of friction, see section 2), and upper crustal rheology with effective viscosity, based on the Wet Quartz flow law [Gleason and Tullis, 1995], WQ, scaled up by 1, 5 or scaled down by 2 or 3; see section 2. Line above model surface indicates denudation front; marker grid is removed where strongly deformed; arrows show flow direction; (8) indicates the suture; and (9) indicates structures resembling north Himalayan gneiss domes.

**Figure 13.** Thermal evolution of models corresponding to those shown in Figure 12 ( $V=H$ ). Panels show isotherms contoured at  $100^\circ\text{C}$  intervals, velocity vectors (short dark lines), and thermal layers (grey =  $A_1$  and white =  $A_2$ ). Other properties are described in Figure 12.

**Figure 14.** Crustal-scale deformation and thermal evolution of model HT-HET ( $V=H$ ) which is similar to HT1 but in which the lower crust comprises a series of 200 km long regions with alternating effective viscosities based on Dry Maryland Diabase (DMD = white and  $\text{DMD}/10 =$

dark grey, Table 1). Upper panel in each set shows deformed marker grid and mechanical layers (grey = middle crustal layer); lower panel shows isotherms (contoured at 100°C intervals), velocity vectors (short dark lines), and thermal layers (grey =  $A_I$  layer). Heavy line with dots represents the position of the model suture (vertical marker '0'). Also shown is distribution and rate of slope-dependent erosion across the model surface; scale maximum = 1 cm/y. Panels a-d show the pro- and retro-crusts at  $t = 30$  and 48 My corresponding to total convergence,  $\Delta x$  of 1500 and 2400 km. Note heterogeneous deformation and mixing despite apparent laminar flow regime.

**Figure 15.** Crustal-scale deformation and thermal evolution of model HT-PS, which is similar to HT1 except the basal boundary condition to a distance of 500 km on either side of the suture corresponds to pure shear thickening of lithospheric mantle (see arrows indicating basal velocities) and there is no subduction of the lower crust ( $V=H$ ). Upper panel in each set shows deformed marker grid and mechanical layers (grey = mid crust); lower panel shows isotherms (contoured at 100 C deg intervals), velocity vectors (short dark lines), and thermal layers (grey =  $A_I$ ). heavy line with dots represents the position of the model suture (vertical marker '0'). Also shown is distribution of slope-dependent erosion across the model surface; scale maximum = 1 cm/y. Panels a-d show the pro- and retro-crusts at  $t = 30$  and 48 My corresponding to total convergence,  $\Delta x$  of 1500 and 2400 km. Note development of mid-crustal channel flows that decouple upper and lower crust and associated near-isothermal, disequilibrium thermal conditions in the mid and lower crust.

**Figure 16.** Diagram showing conceptual interpretation of a range of model crustal flow modes that lead to uplift, exhumation, folding, extrusion and doming mechanisms. Panels show weak upper

crust (white), mid crust (grey), lower crust (white), and currently (pattern) or formerly (stipple) melt-weakened crust.

**Figure 17.** Illustration of a representative north-south tectonic cross section of the Himalaya and southern Tibet showing the processes that act together to provide an internally consistent explanation for the dynamical behavior of this system. This system behavior is seen in model HT1 (Fig. 10), for example, and in variants (Figs. 12 and 13). See text for explanation of numbers. MBT = Main Boundary Thrust, FTB = fold-thrust belt (Siwaliks), MCT = Main Central Thrust system, GHS = Greater Himalayan sequence (stippled pattern), STD = South Tibetan Detachment system, LHS = Lesser Himalayan sequence, MHT = Main Himalayan Thrust (Modified from Beaumont et al., 2001b).

**Table 1.** Parameters used in models (see also Figure 1).

Parameter	Meaning	Value(s)
Parameters and nominal values		
a) Mechanical parameters		
$\rho_{crust}$	crustal density	2700 kg/m <sup>3</sup>
$\rho_{mantle}$	mantle density	3300/3200 kg/m <sup>3</sup>
$D$	flexural rigidity (isostasy model)	10 <sup>22</sup> Nm
	crustal thickness	35 km
	lower crustal thickness	10 km
$\theta$	subduction dip angle	20°
$\phi_{eff}$	effective internal angle of friction	15°
$C$	cohesion	10 MPa
$P$	solid pressure	Pa
$J_2^I$	second invariant of the deviatoric stress tensor	Pa <sup>2</sup>
$\eta_{eff}^v = B^* \cdot (\dot{I}_2^I)^{(1-n)/2n} \cdot \exp[Q/nRT_K]$	general equation for effective viscosity	
$\dot{I}_2^I$	second invariant of strain rate tensor	s <sup>-2</sup>
$R$	gas constant	8.314 J/mol°K
$T_K$	absolute temperature	°K
$B^*, n, Q$ as below		
WQ	wet Black Hills quartzite flow law [after <i>Gleason and Tullis</i> , 1995]	$n = 4.0$ $B^* = 2.92 \times 10^6 \text{ Pa}\cdot\text{s}^{1/4}$ $Q = 223 \text{ kJ/mol}$
WQ x 5 (etc.)	modified wet Black Hills quartzite flow law	$B^* = B^* \text{ (WQ)} \times 5 \text{ (etc.)}$
DMD	dry Maryland diabase flow law [after <i>Mackwell et al.</i> , 1998]	$n = 4.7$ $B^* = 1.91 \times 10^5 \text{ Pa}\cdot\text{s}^{1/4.7}$ $Q = 485 \text{ kJ/mol}$
DMD/10	modified dry Maryland diabase flow law	$B^* = B^* \text{ (DMD)} / 10$
'melt weakening'	linear reduction in effective viscosity over T range 700-750°C for WQ only	$\eta_{700} = \text{flow law value}$ $\eta_{750} = 10^{19} \text{ Pa}\cdot\text{s}$
	length of Eulerian model domain	2000 km
b) Basal velocity boundary conditions		
Type-1 models		
$V_P$	pro-side (convergence) velocity	2 cm/y
$V_R$	retro-side velocity	0 cm/y
$V_S$	S-point velocity (subduction advance)	0 cm/y
Type-2 models		
$V_P$	pro-side (convergence) velocity	5 cm/y
$V_R$	retro-side velocity	0 cm/y
$V_S$	S-point velocity (subduction advance)	2.5 cm/y

c) Thermal parameters

$K$	thermal conductivity	2.00 W/m <sup>2</sup> K
$\kappa$	thermal diffusivity ( $\kappa = K / \rho C_p$ , where $\rho C_p = 2 \times 10^6$ )	$1.0 \times 10^{-6}$ m <sup>2</sup> /s
$T_s$	surface temperature	0°C
$T_a$	temperature at lithosphere/ asthenosphere boundary	1350°C
$q_m$	basal mantle heat flux	20 mW/m <sup>2</sup>
$q_s$	initial surface heat flux	71.25 mW/m <sup>2</sup>
$A_1$ (0-20 km)	upper crustal heat production	$2.0 \mu\text{W/m}^3$
$A_2$ (20-35 km)	lower crustal heat production	$0.75 \mu\text{W/m}^3$

d) Surface denudation

slope x $f(t)$ x $g(x)$	denudation rate (m/y)	
slope	local surface slope (see text)	
$f(t)$	time function	
	specifies how denudation rate (m/y) varies with time when $g(x)$ and slope = 1	
$g(x)$	spatial function	
	specifies how denudation rate varies with position $x$	$g(x) = 0 =$ arid $g(x) = 1 =$ wet

e) Specific model parameters

Type-1 models (no subduction of lower crust)

Model 1

$\phi_{eff}$ (0-35 km)		15°
WQ x 5 (0-25 km)		
DMD (25-35 km)		
‘melt weakening’		
$f(t)$	0.0	$t \leq 37.5$ My
	varies linearly 0.0 → 0.107 m/y	$37.5 < t < 45$ My
	0.107 m/y	$45 \leq t \leq 75$ My
	e.g. gives denudation rate of 1.07 cm/y when slope = 1:10 and $g(x) = 1.0$	
$g(x)$	1.0	$0 < x \leq 450$ km
	varies linearly 1.0 → 0.0	$450 < x < 500$ km
	0.0	$x \geq 500$ km

Model 2

as Model 1 but no erosion

$f(t)$	0	$t > 0$
$g(x)$	0	$t > 0$

Model 3

as Model 1 but no ‘melt weakening’

Model 4

as Model 1 but minimum 'melt weakened' viscosity

$2 \times 10^{18}$  Pa.s

Model 5

as Model 1 except

$\phi_{eff}$  (0-35km)

$5^\circ$

Type-2 models

Model HT1 (subduction of lower crust)

$\phi_{eff}$  (0-10 km)

$5^\circ$

$\phi_{eff}$  (10-25 km)

$15^\circ$

WQ (0-10 km)

WQ x 5 (10-25 km)

DMD (25-35 km)

$f(t)$

0.0  
varies linearly 0.0  $\rightarrow$  0.133 m/y  
0.133 m/y  
varies linearly 0.133  $\rightarrow$  0.04 m/y  
0.04 m/y

$t \leq 24$  My  
 $24 < t < 27$  My  
 $27 \leq t \leq 39$  My  
 $39 < t < 48$  My  
 $48 \leq t \leq 54$  My

$g(x)$

1.0  
varies linearly 1.0  $\rightarrow$  0.0  
0.0

$0 < x \leq 500$  km  
 $500 < x < 550$  km  
 $x \geq 550$  km

Model HT-HET (no subduction of lower crust)

as Model HT1 but lower crust comprises alternating 200 km regions of

DMD (25-35 km)

DMD/10 (25-35 km)

$f(t)$

same as Model HT1

$g(x)$

same as Model HT1

Model HT-PS (no subduction of lower crust)

as Model HT1 but basal velocity boundary conditions

$V$  (0-400 km)

5 cm/y

$V$  (400-1400 km) linear decrease

5  $\rightarrow$  0 cm/y

$V$  (1400-2000 km)

0 cm/y

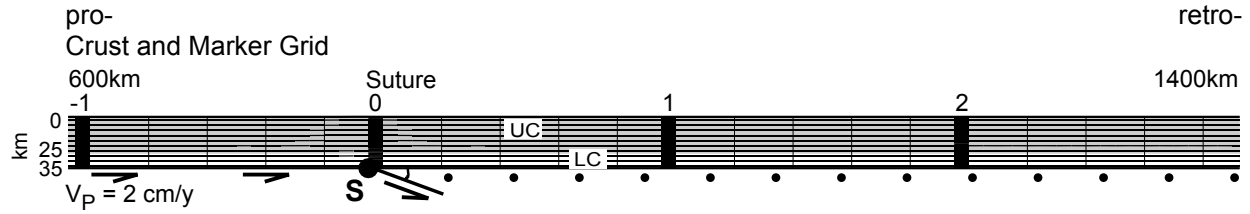
$f(t)$

same as Model HT1

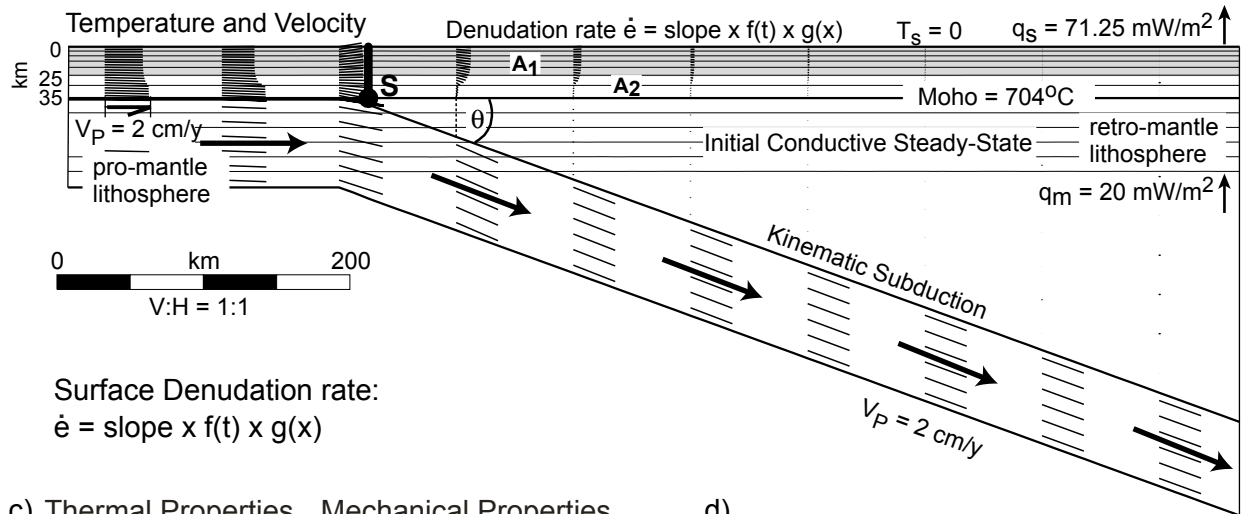
$g(x)$

same as Model HT1

a) Mechanical Model

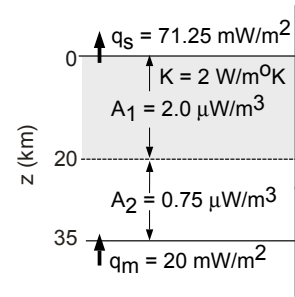


b) Thermal Model

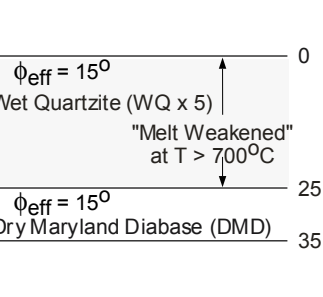


Surface Denudation rate:  
 $\dot{\epsilon} = \text{slope} \times f(t) \times g(x)$

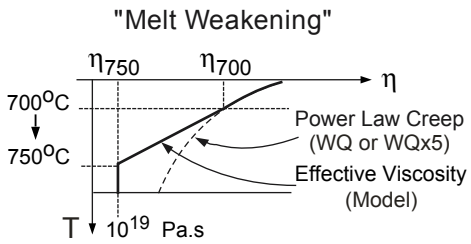
c) Thermal Properties



Mechanical Properties



d)



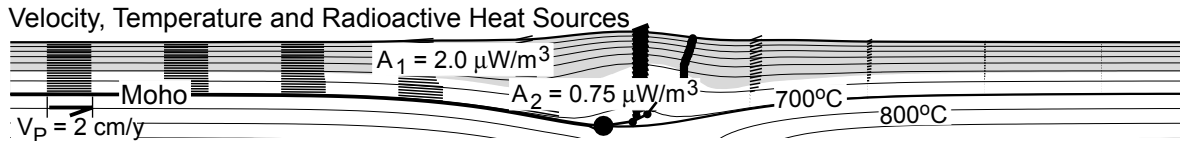
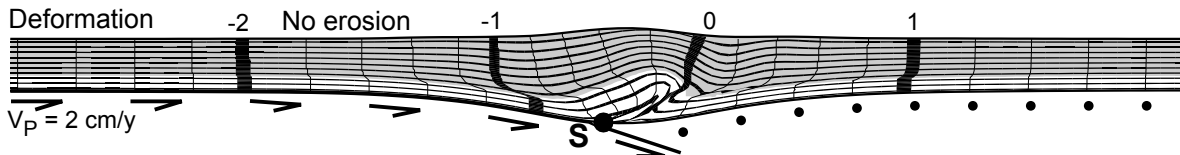
Beaumont et al., FIGURE 1

Model 1: 0 - 30 My

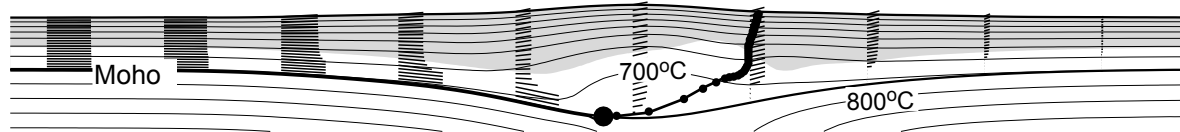
pro-

retro-

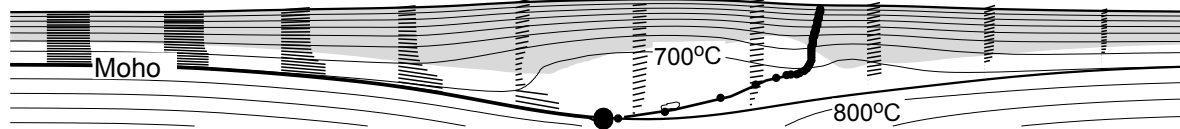
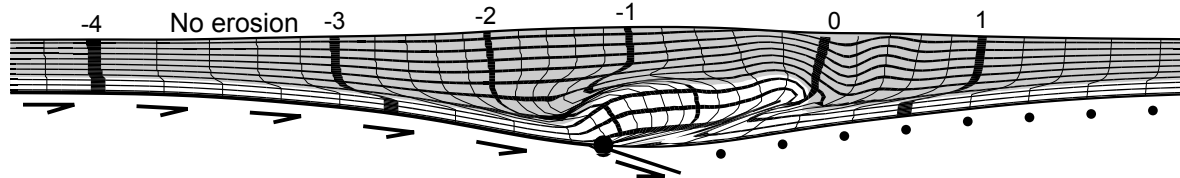
a)  $t = 7.5$  My;  $\Delta x = 150$  km



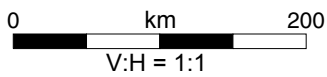
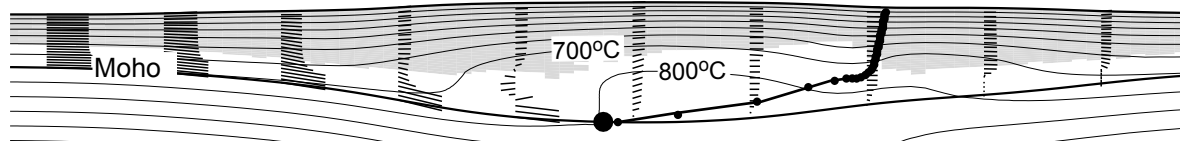
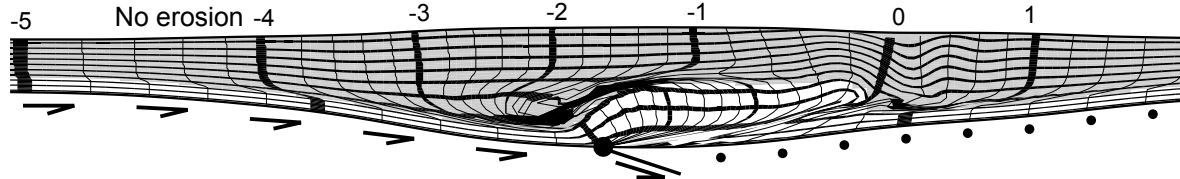
b)  $t = 15$  My;  $\Delta x = 300$  km



c)  $t = 22.5$  My;  $\Delta x = 450$  km



d)  $t = 30$  My;  $\Delta x = 600$  km



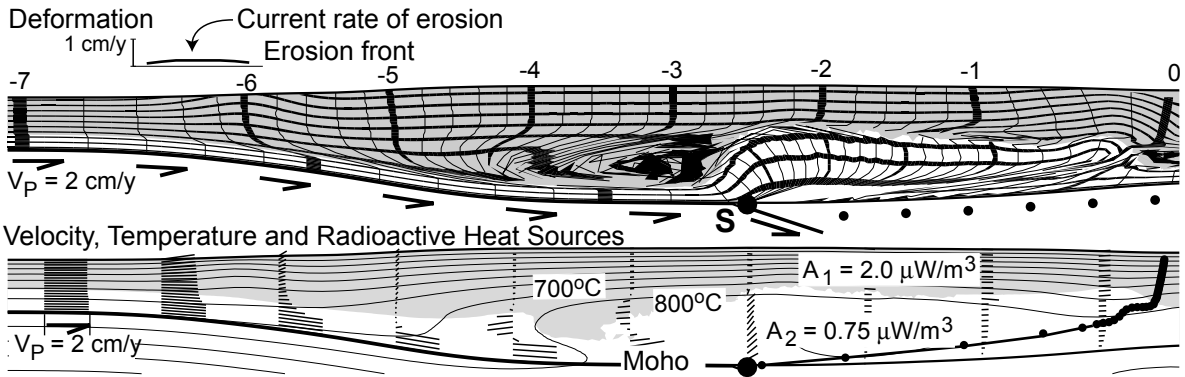
Beaumont et al., FIGURE 2

Model 1: 45 - 60 My

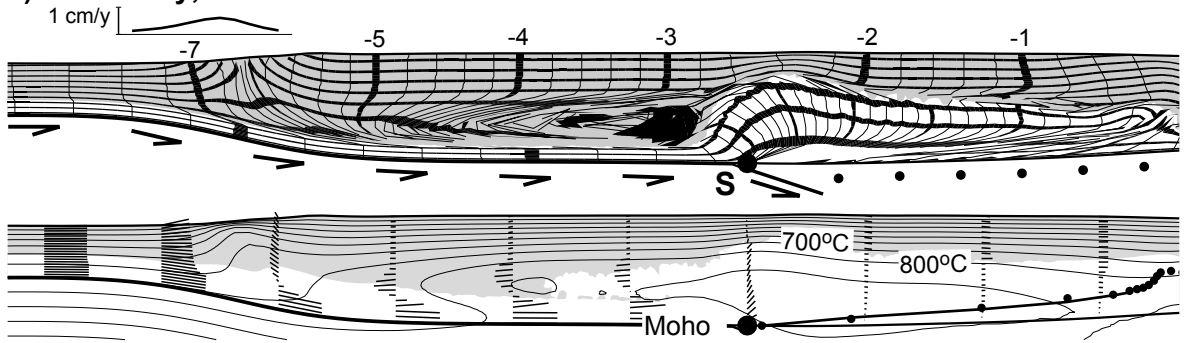
pro-

retro-

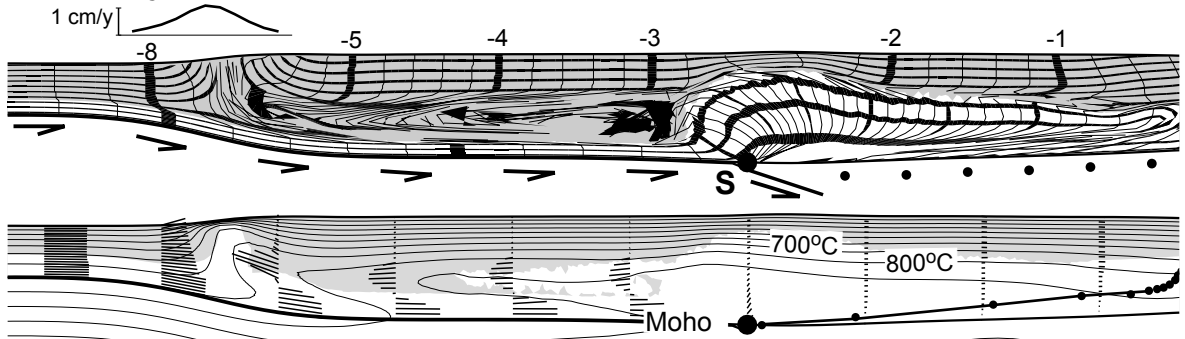
a)  $t = 45 \text{ My}$ ;  $\Delta x = 900 \text{ km}$



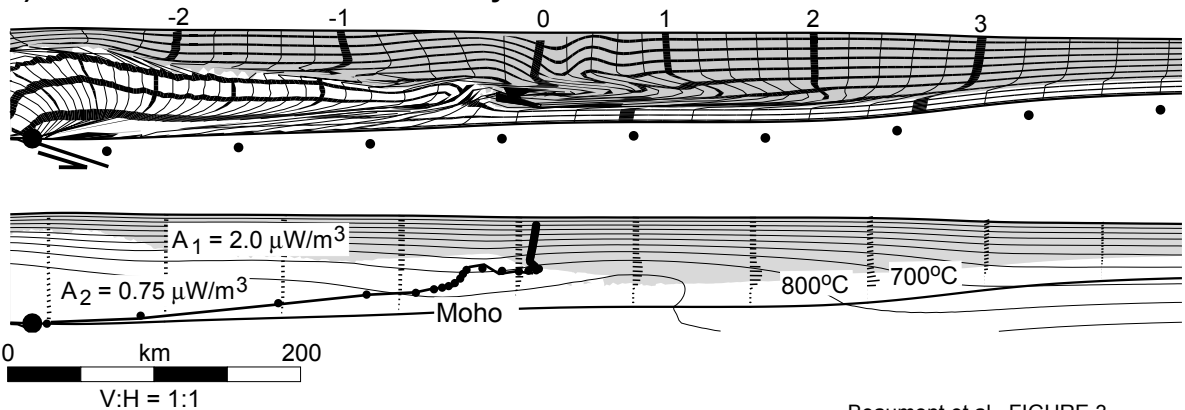
b)  $t = 52.5 \text{ My}$ ;  $\Delta x = 1050 \text{ km}$

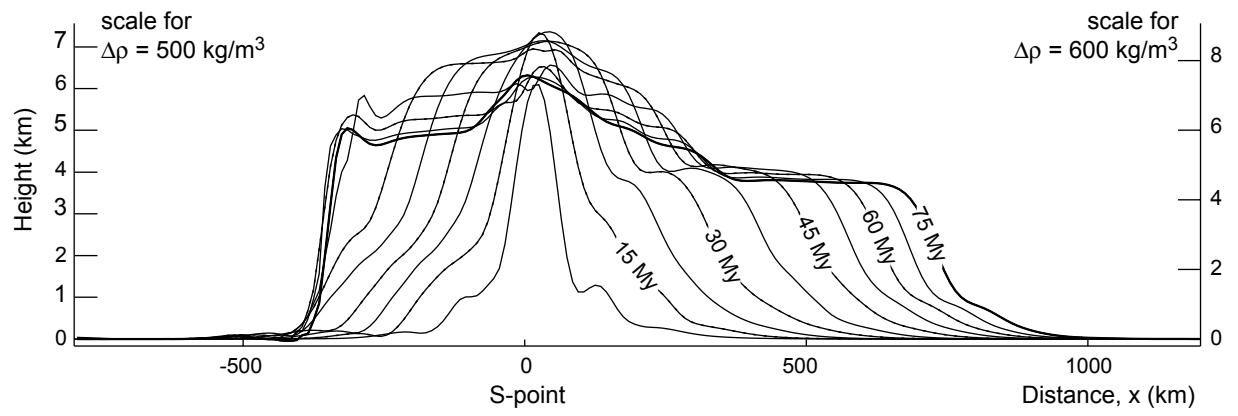


c)  $t = 60 \text{ My}$ ;  $\Delta x = 1200 \text{ km}$



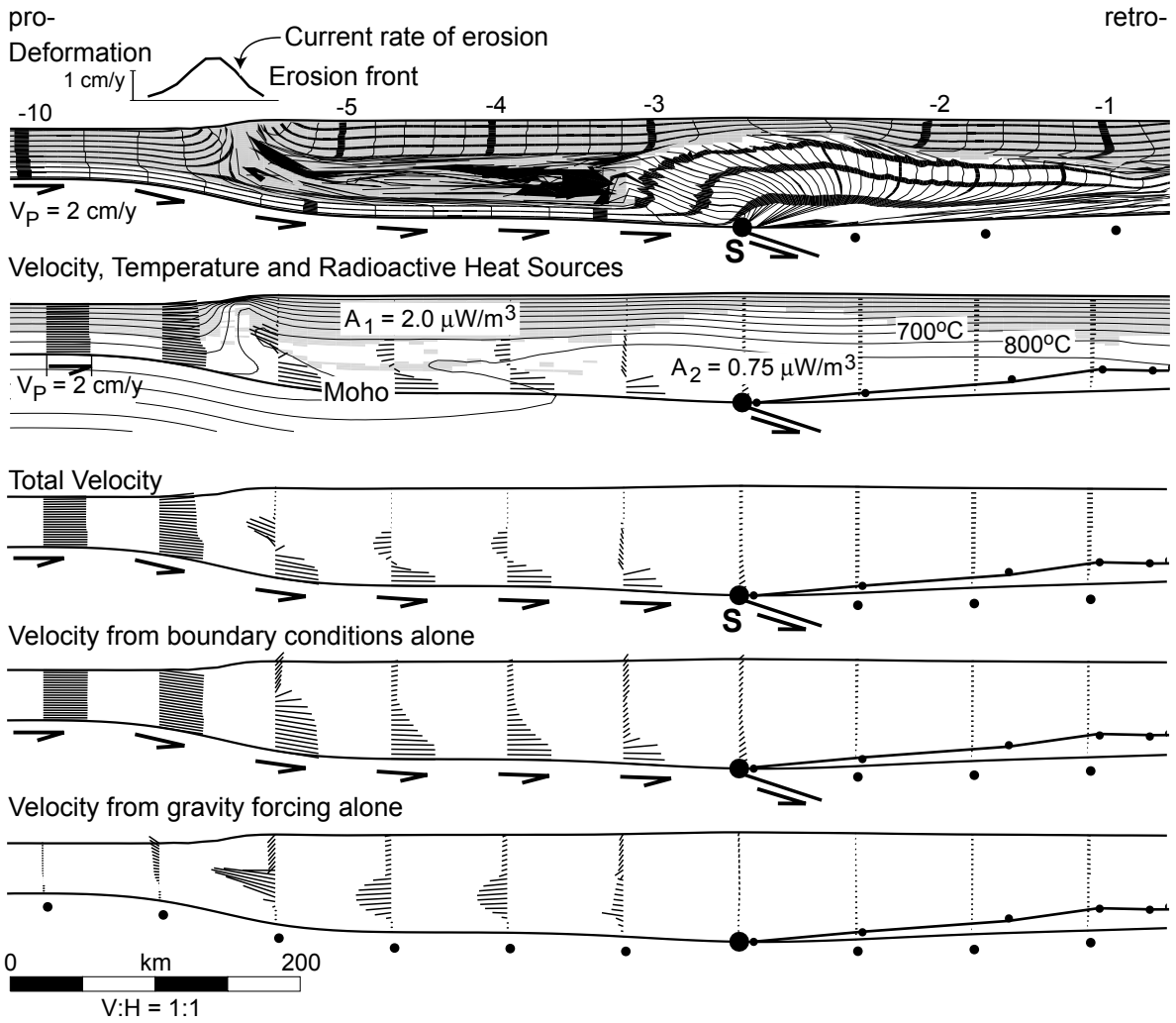
d) Retro-side of Model 1 at  $t = 60 \text{ My}$





Beaumont et al., FIGURE 4

Model 1:  $t = 75 \text{ My}$ ;  $\Delta x = 1500 \text{ km}$



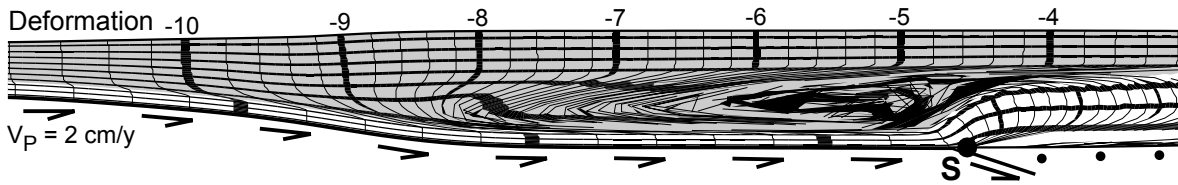
Beaumont et al., FIGURE 5

Models 2, 3, 4:  $t = 75 \text{ My}$ ;  $\Delta x = 1500 \text{ km}$

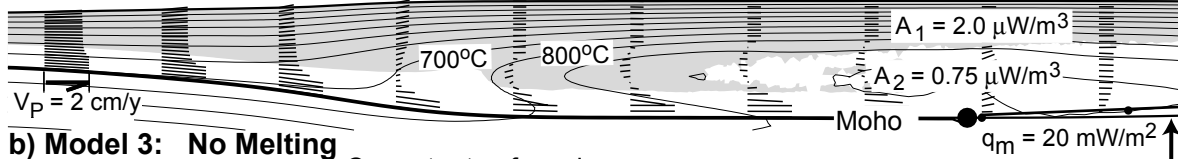
pro-

retro-

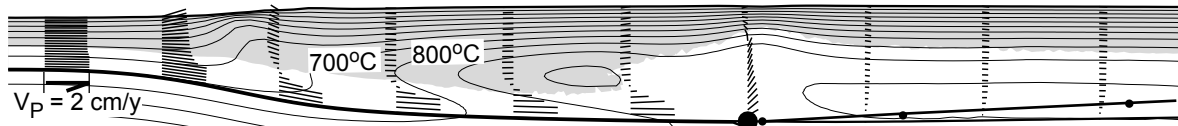
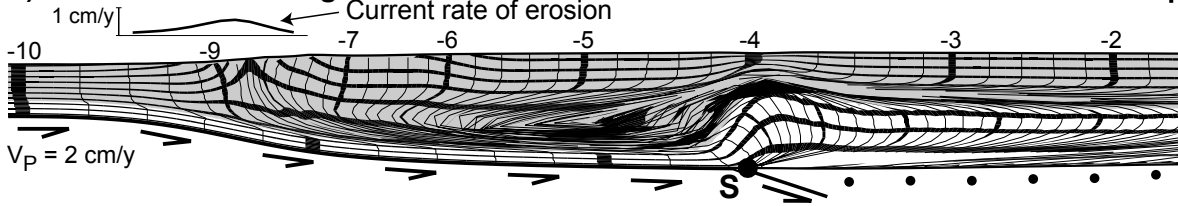
**a) Model 2: No Erosion**



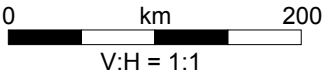
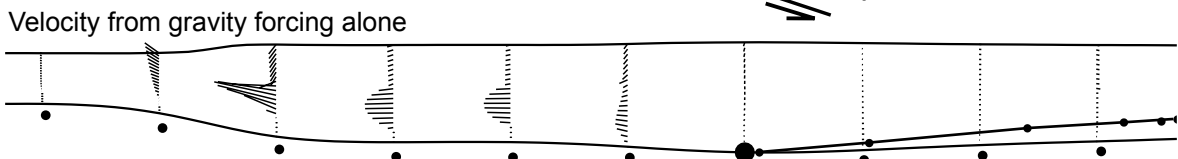
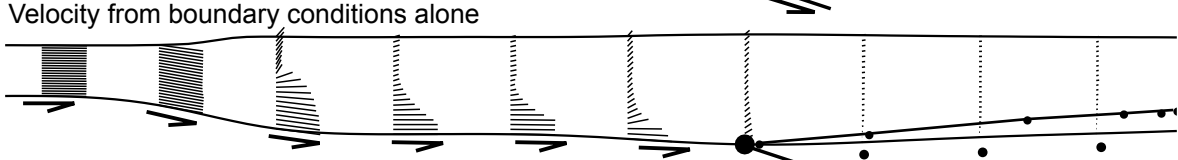
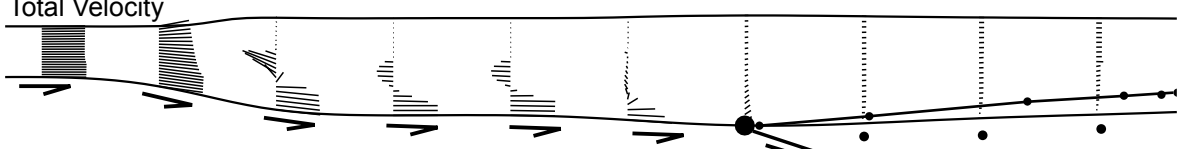
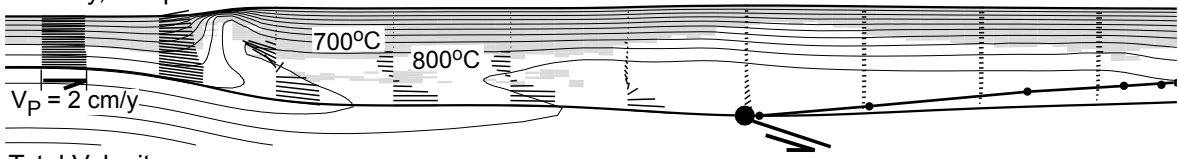
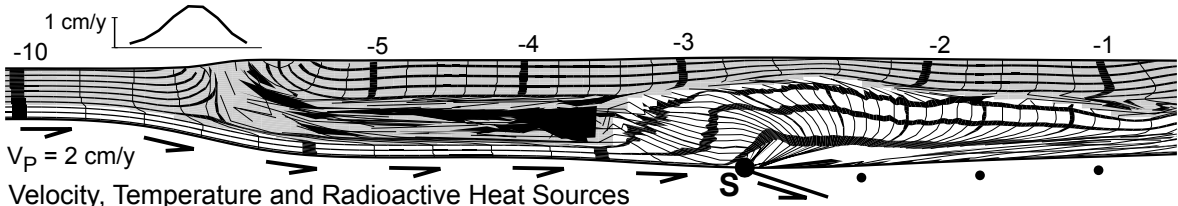
Velocity, Temperature and Radioactive Heat Sources



**b) Model 3: No Melting**

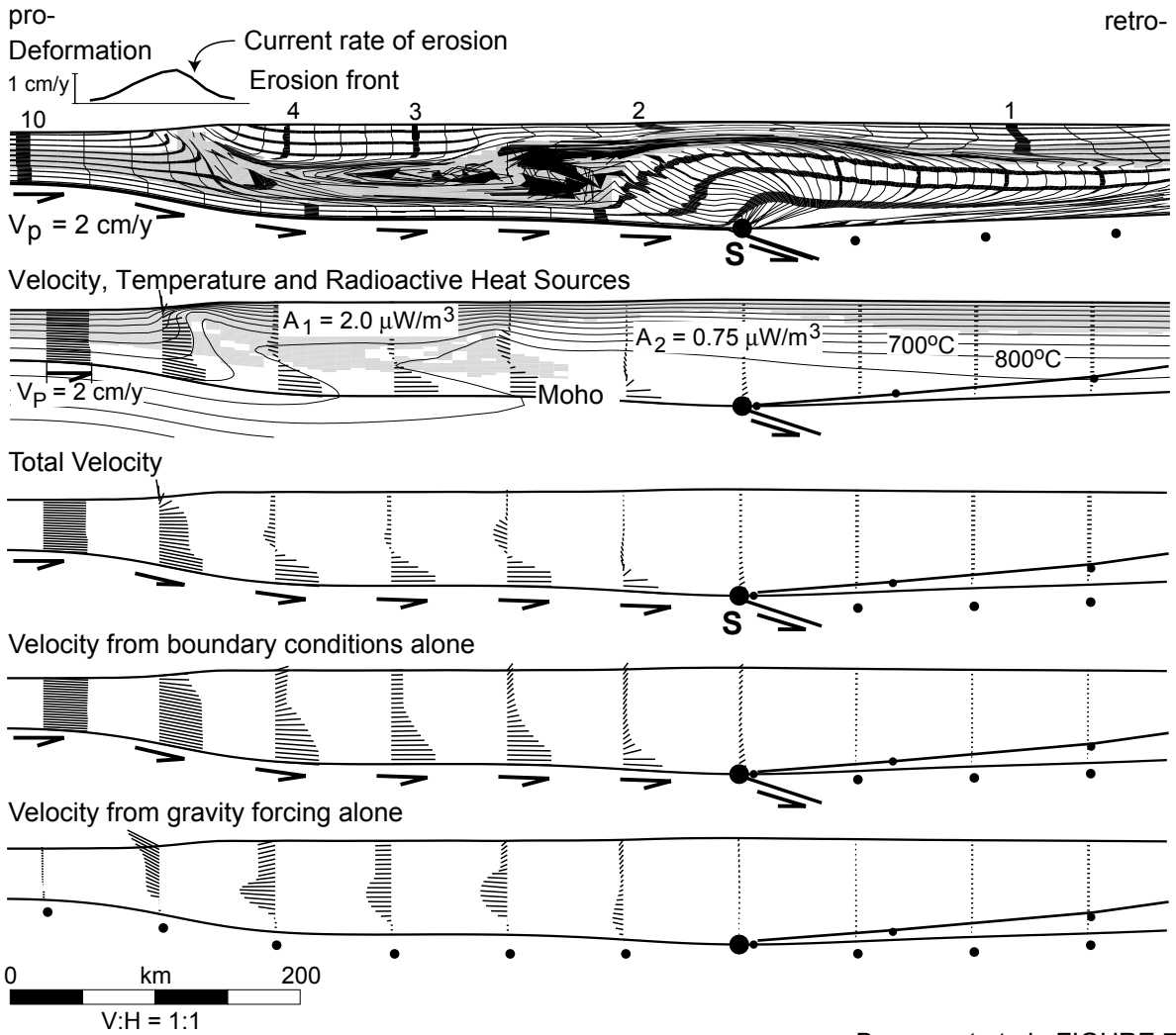


**c) Model 4: Lower Viscosity Channel ( $\eta_{750} = 2 \times 10^{18} \text{ Pa.s.}$ )**



Beaumont et al., FIGURE 6

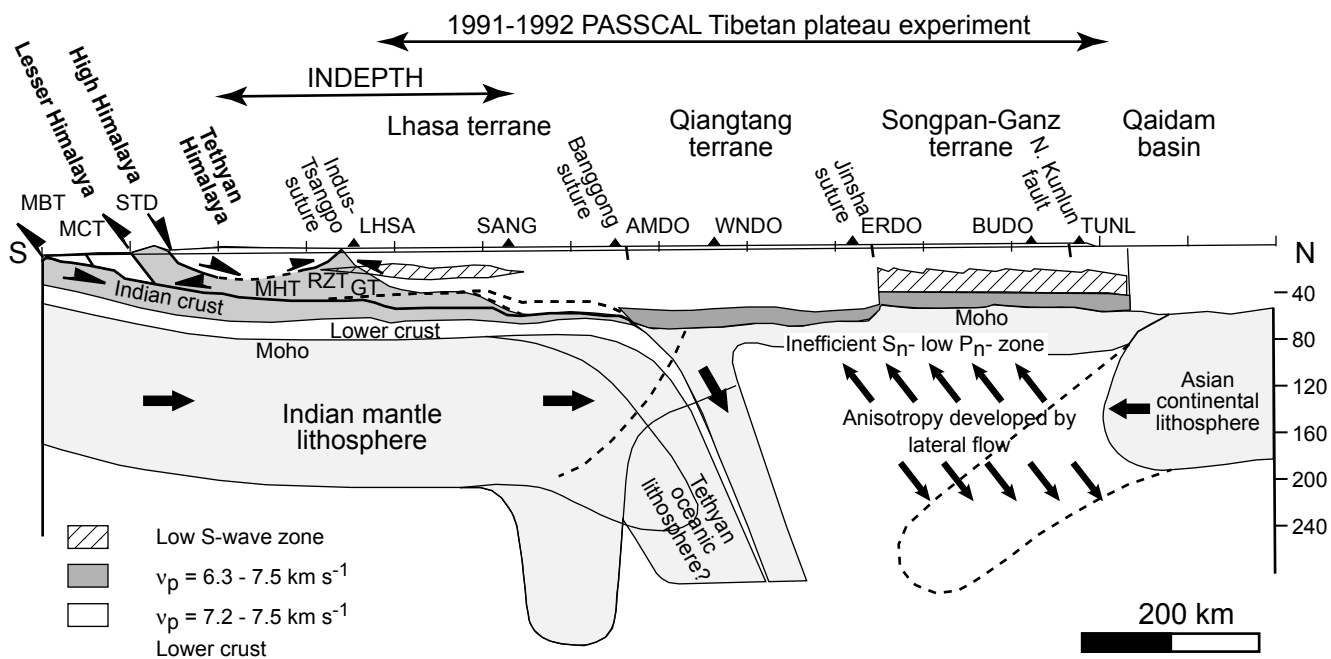
Model 5:  $t = 75 \text{ My}$ ;  $\Delta x = 1500 \text{ km}$



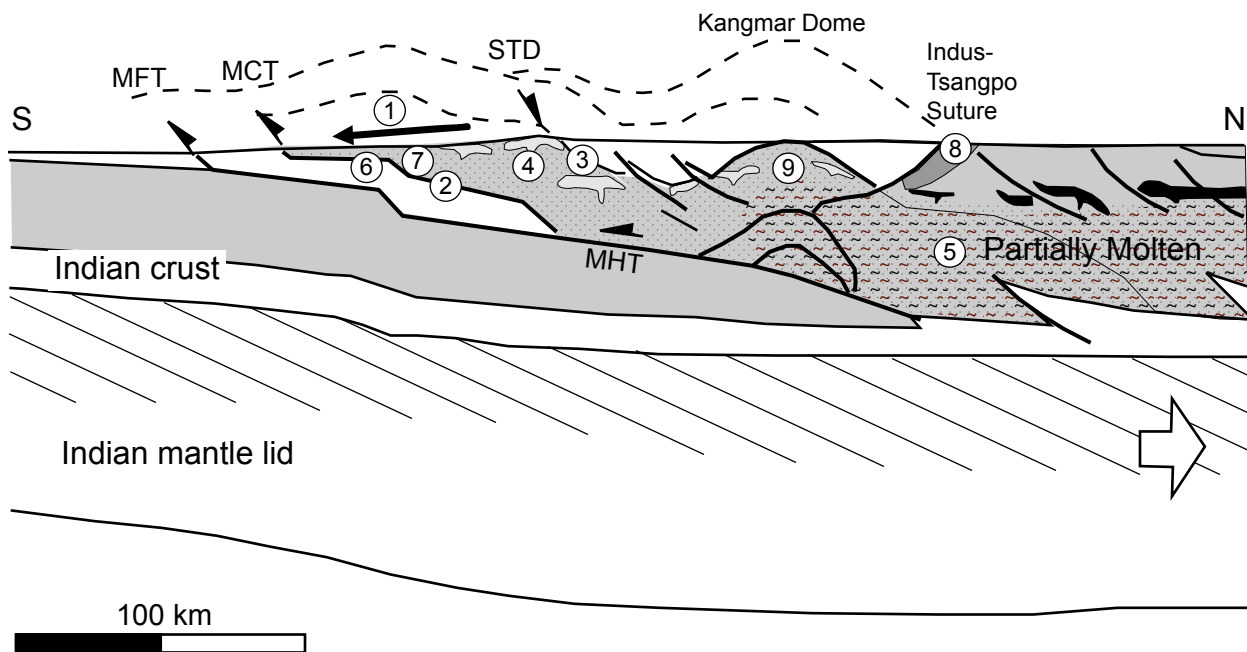
Beaumont et al., FIGURE 7

# Cross Section of Himalayan-Tibetan Orogen

a)

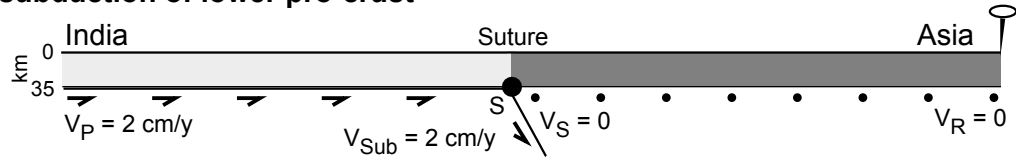


b)

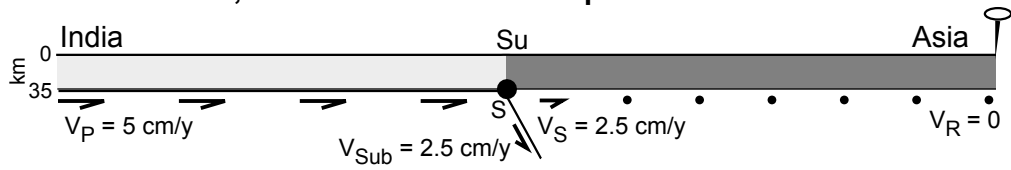


Beaumont et al., FIGURE 8

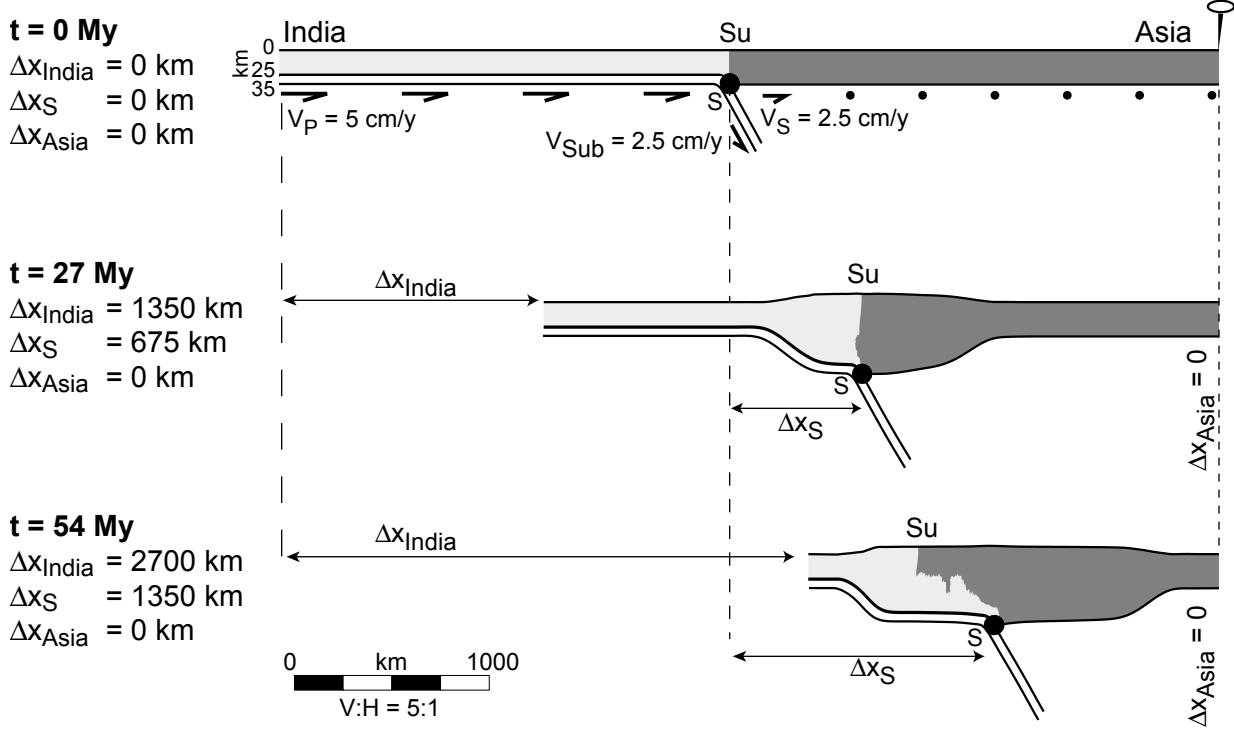
**a) Model 1, No subduction of lower pro-crust**



**b) Advancing Subduction Model, No subduction of lower pro-crust**



**c) Model HT1, Advancing Subduction Model, with subduction of lower pro-crust**



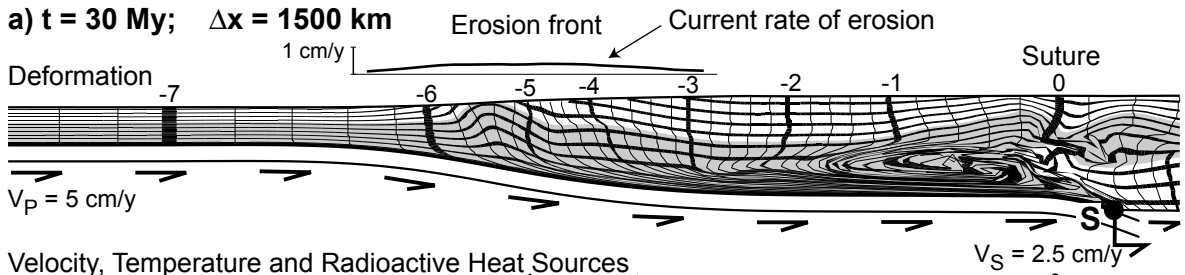
Beaumont et al., FIGURE 9

# Model HT1

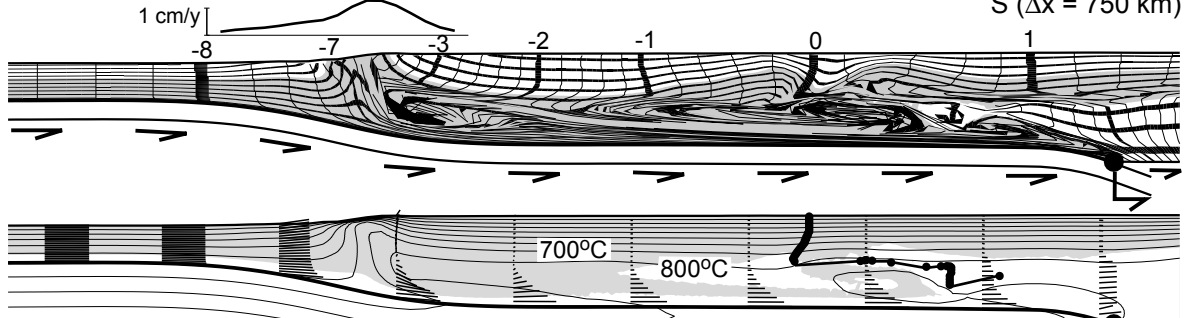
pro-

retro-

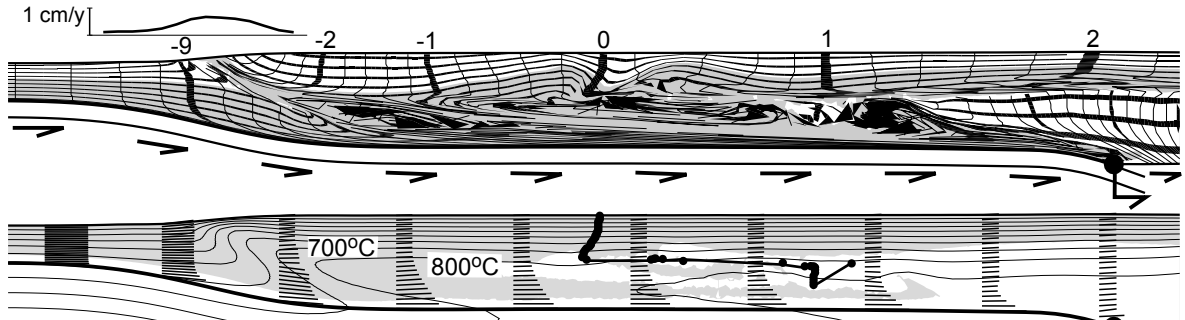
**a) t = 30 My; Δx = 1500 km**



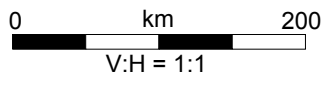
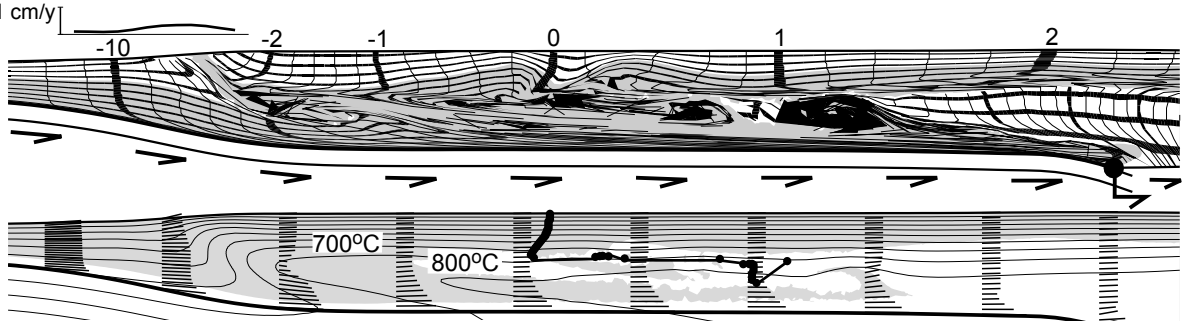
**b) t = 39 My; Δx = 1950 km**



**c) t = 48 My; Δx = 2400 km**

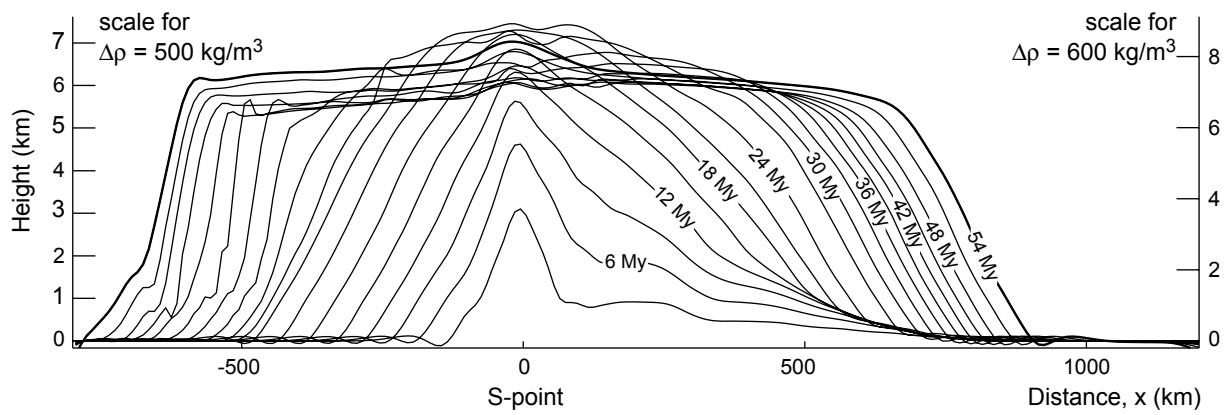


**d) t = 54 My; Δx = 2700 km**

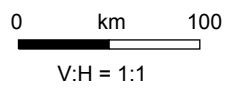
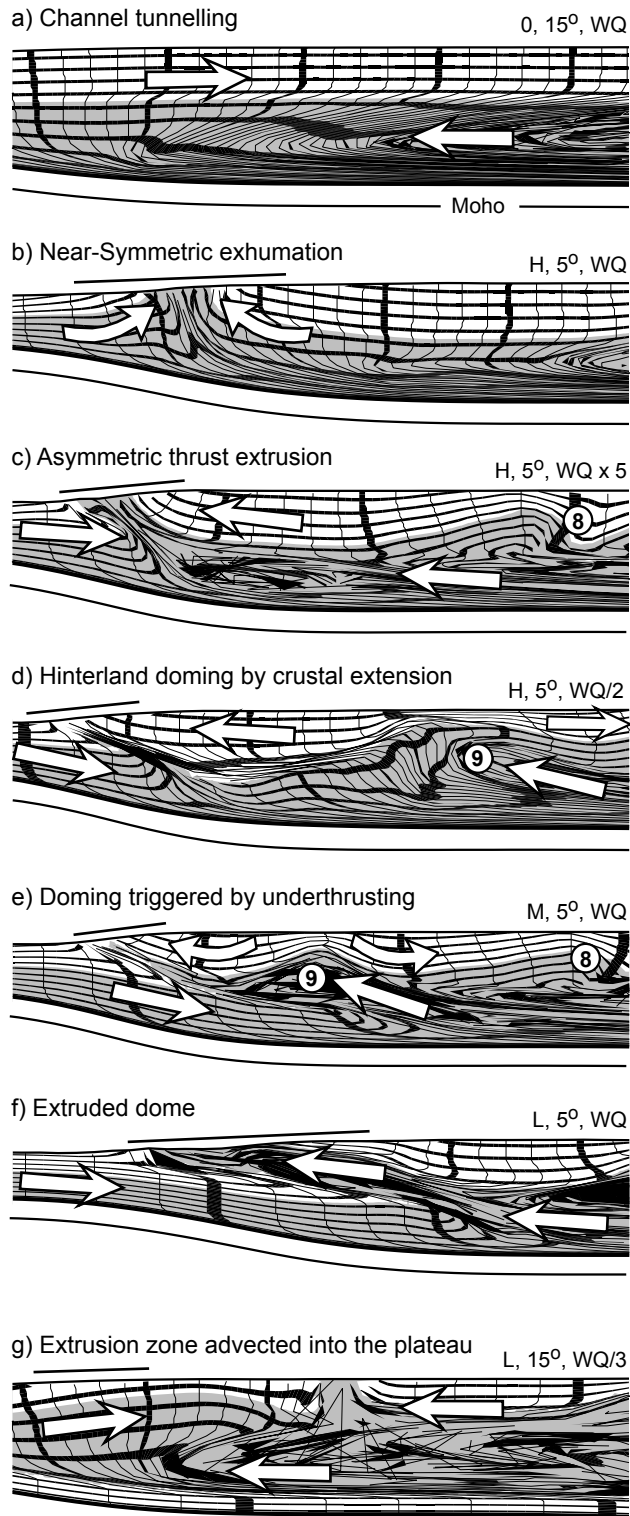


S (Δx = 1350 km)

Beaumont et al., FIGURE 10

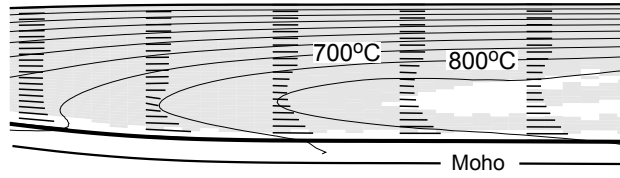


Beaumont et al., FIGURE 11

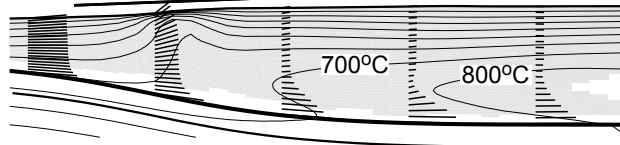


Beaumont et al., FIGURE 12

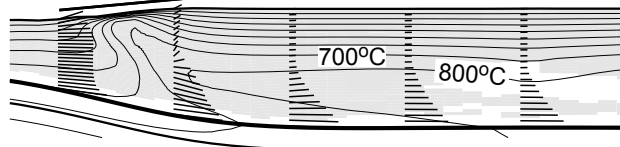
a) Channel tunnelling 0, 15°, WQ



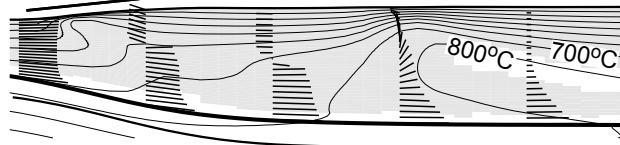
b) Near-Symmetric exhumation H, 5°, WQ



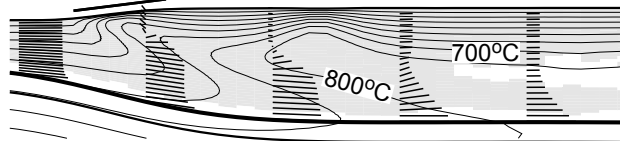
c) Asymmetric thrust extrusion H, 5°, WQ x 5



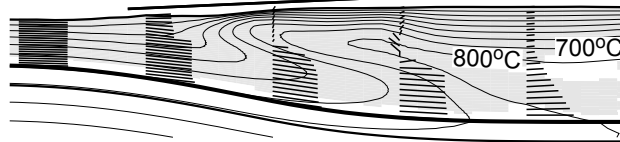
d) Hinterland doming by crustal extension H, 5°, WQ/2



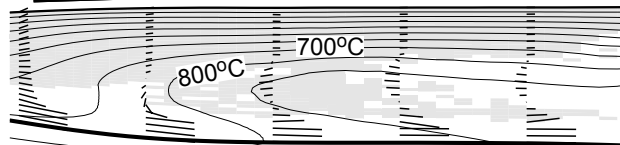
e) Doming triggered by underthrusting M, 5°, WQ



f) Extruded dome L, 5°, WQ



g) Extrusion zone advected into the plateau L, 15°, WQ/3



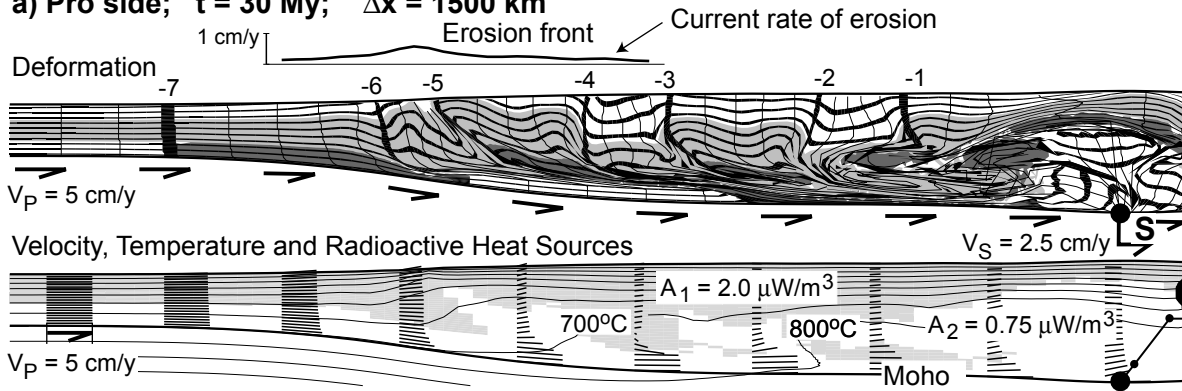
0 km 100

V:H = 1:1

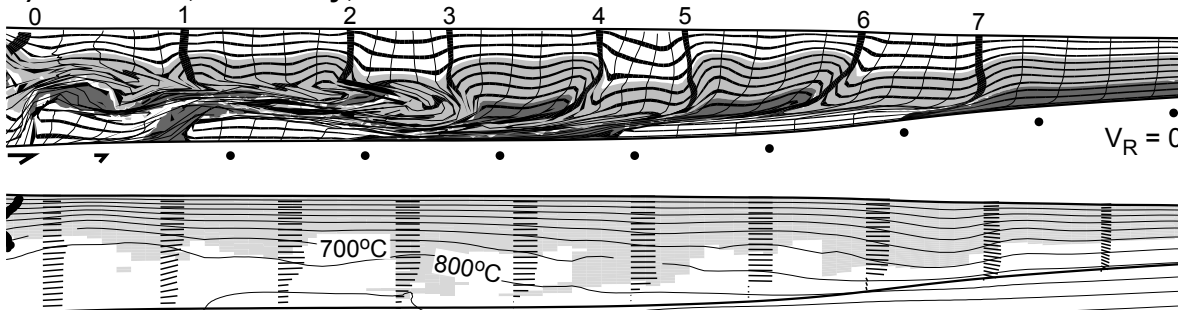
Beaumont et al., FIGURE 13

# Model HT-HET

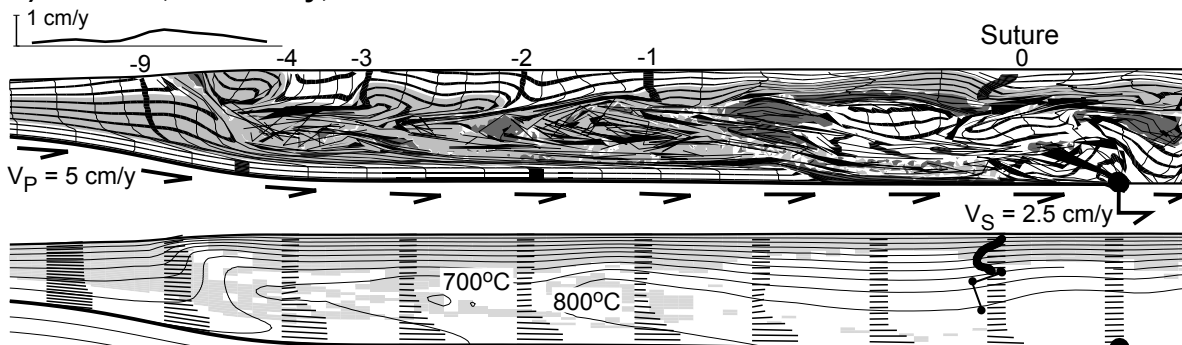
**a) Pro side;  $t = 30$  My;  $\Delta x = 1500$  km**



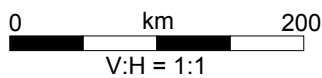
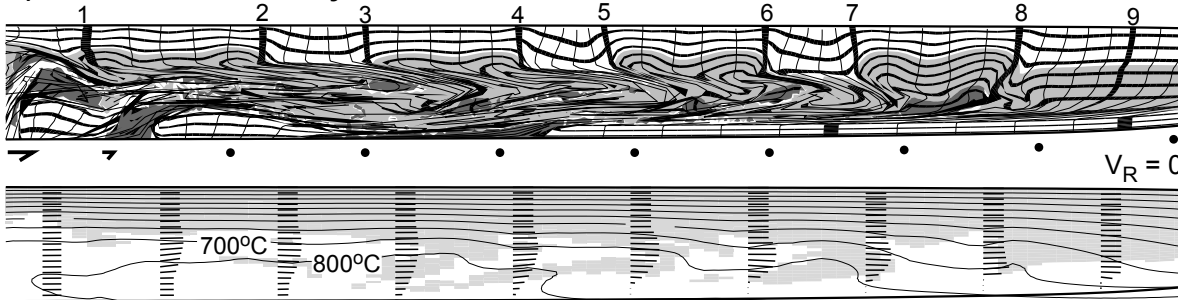
**b) Retro side;  $t = 30$  My;  $\Delta x = 1500$  km**



**c) Pro side;  $t = 48$  My;  $\Delta x = 2400$  km**

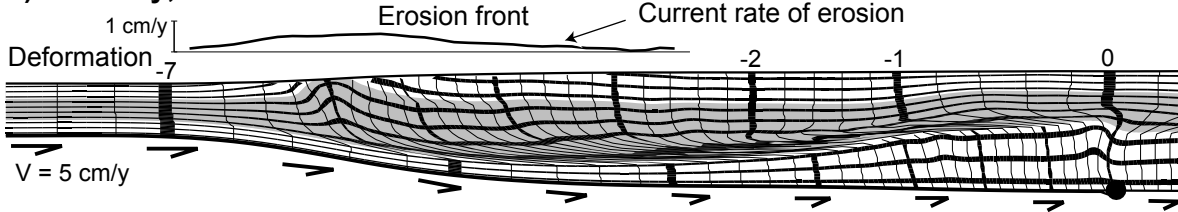


**d) Retro side;  $t = 48$  My;  $\Delta x = 2400$  km**

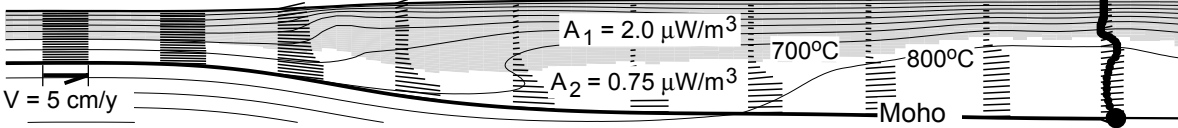


# Model HT-PS

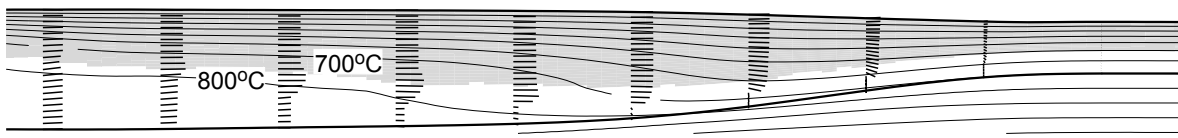
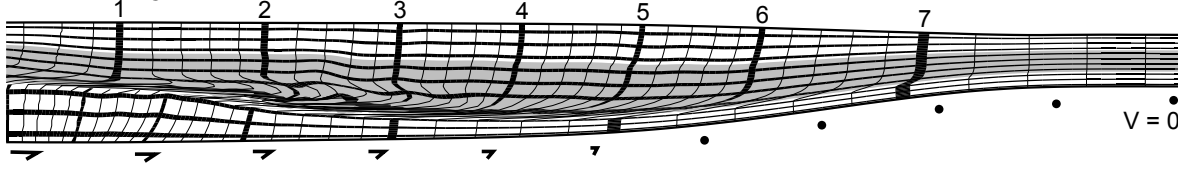
a)  $t = 30 \text{ My}$ ;  $\Delta x = 1500 \text{ km}$



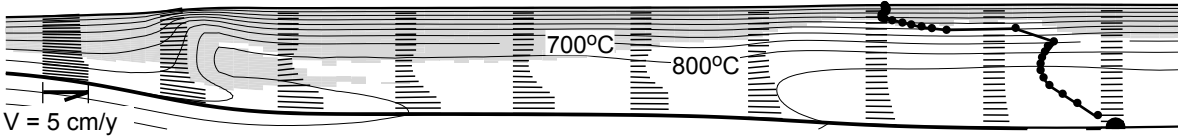
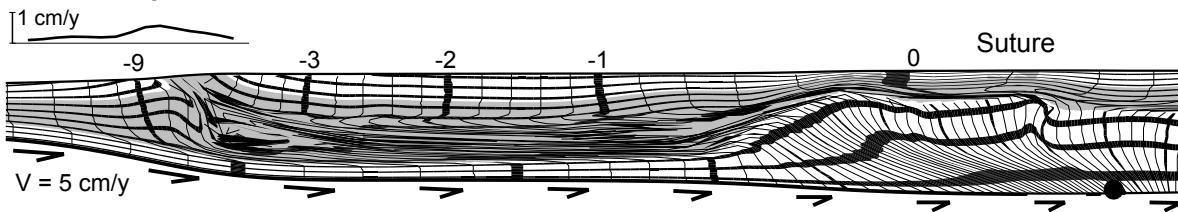
Velocity, Temperature and Radioactive Heat Sources



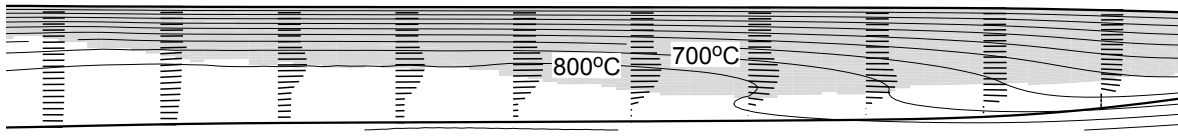
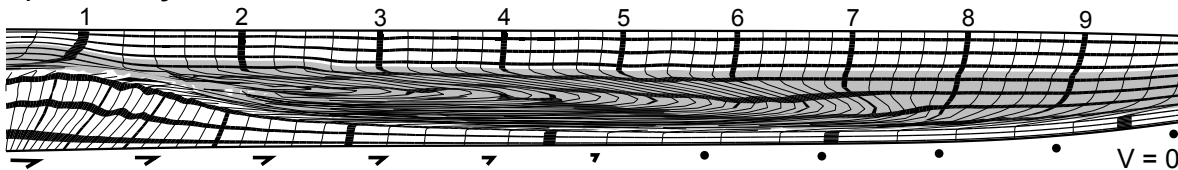
b)  $t = 30 \text{ My}$ ;  $\Delta x = 1500 \text{ km}$



c)  $t = 48 \text{ My}$ ;  $\Delta x = 2400 \text{ km}$

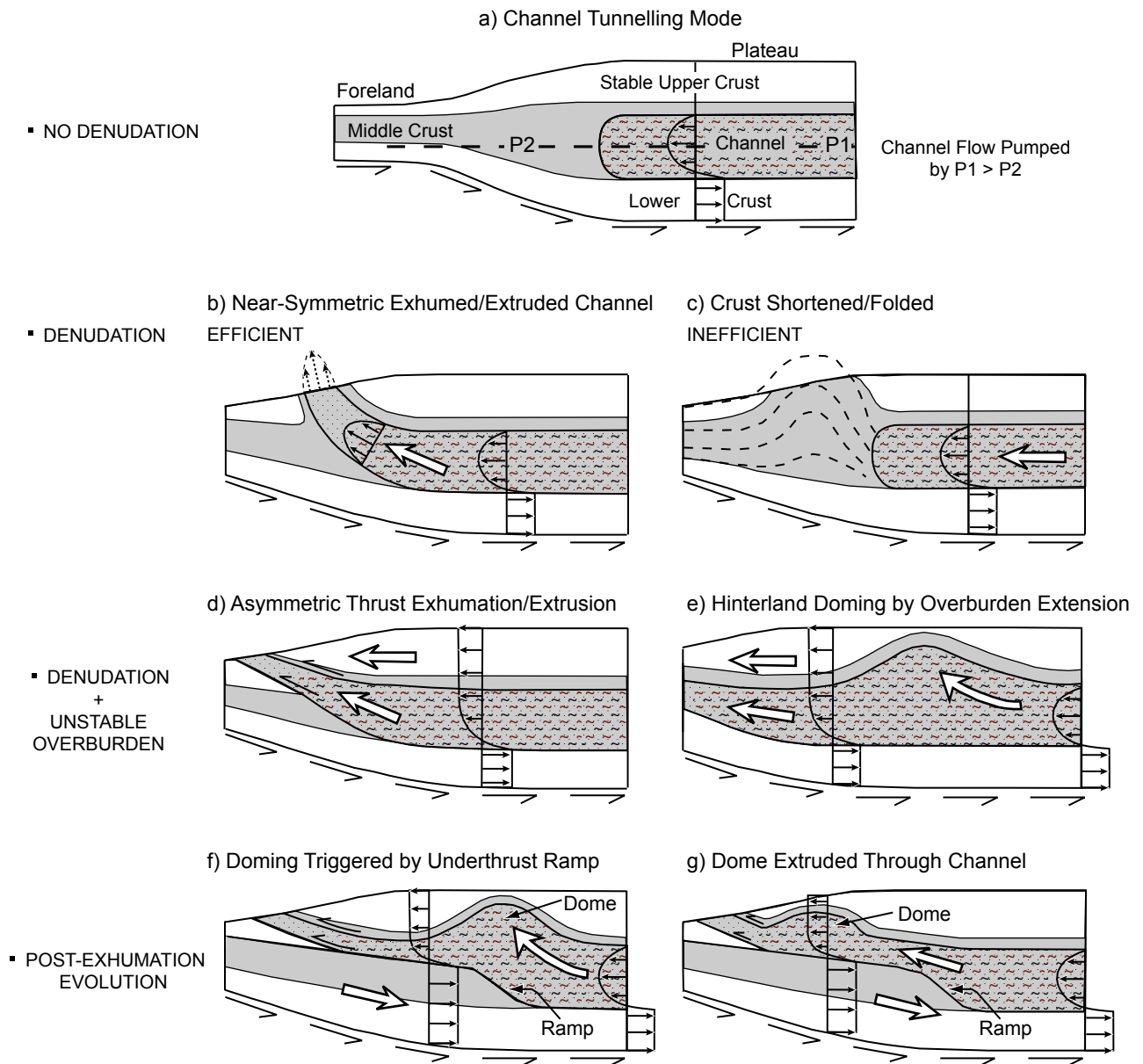


d)  $t = 48 \text{ My}$ ;  $\Delta x = 2400 \text{ km}$

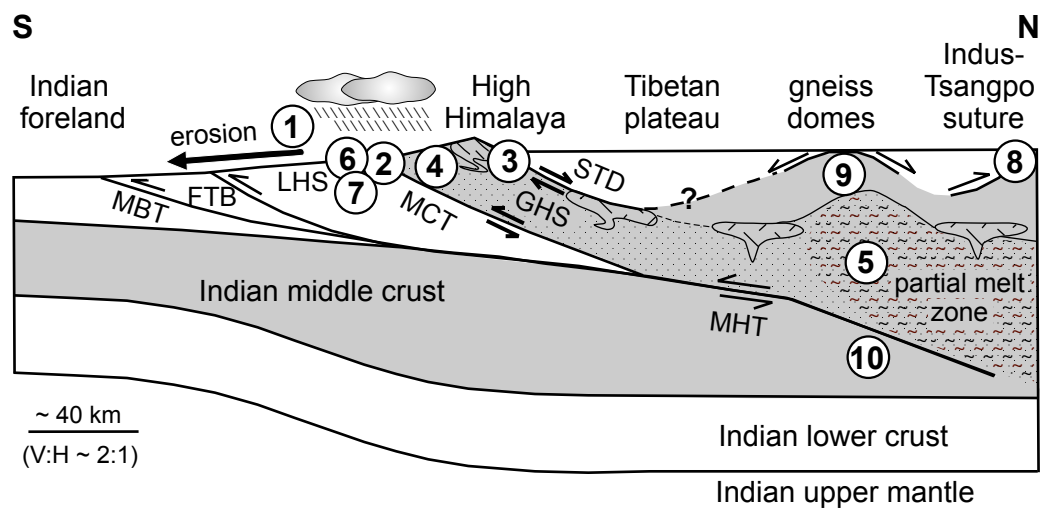


0 km 200

V:H = 1:1



Beaumont et al., FIGURE 16



Beaumont et al., FIGURE 17